# scientific reports



# **OPEN** Synergistic effects of basalt fiber and volcanic pumice powder in high-strength geopolymer concrete

Mohamed Abdellatief<sup>1</sup>, Hassan Hamouda<sup>2</sup>, Martin T. Palou<sup>3</sup> & Taher A. Tawfik<sup>3,4⊠</sup>

This paper explores the synergistic effects of basalt fiber (BF) and volcanic pumice powder (VPP) on the physico-mechanical, thermal characteristics, efflorescence, and microstructure of high-strength geopolymer concrete (HSGC). HSGC mixtures were developed by partially replacing ground granulated blast furnace slag with 0-40% VPP while incorporating BF in the range of 0-1.5%. The experimental findings demonstrate that increasing BF content from 0.75 to 1.5% significantly enhances compressive, flexural, and splitting tensile strengths, with compressive strength increasing by up to 14.51% at 28 days and flexural and splitting strengths improving by 13.17% and 14.46%, respectively. Conversely, higher VPP content generally reduces compressive strength, with a 40% replacement leading to a 23% decline at 7 days. Moreover, while increased BF levels improved the microstructure and thermal stability, higher volumes of VPP were found to deteriorate the microstructure, thereby accelerating the efflorescence process. Particularly, the HSGC sample containing 10% VPP significantly reduced both the crystal area and thickness compared to other mixtures. A multi-objective optimization approach revealed that higher BF content improved HSGC properties, whereas higher VPP levels diminished performance. The optimal HSGC formulation achieved a compressive strength of 59.25 MPa, a splitting strength of 7.51 MPa, a flexural strength of 8.64 MPa, and a dry density of 2012 kg/m<sup>3</sup>, with 0.69% BF and 17.79% VPP. Macroscopic and thermal analyses demonstrated that the optimal HSGC sample exhibited a more compact microstructure, demonstrating the effectiveness of response surface methodology in identifying the ideal mixture parameters for HSGC design.

**Keywords** High strength geopolymer concrete, Volcanic pumice powder, Basalt fiber, Response surface methodology

Portland cement (PC) composites are widely used in infrastructure due to their durability, cost-effectiveness, and design flexibility<sup>1</sup>. However, the traditional production of PC is environmentally detrimental, with high energy demand and substantial CO<sub>2</sub> emissions. Thus, finding sustainable alternatives to PC concrete is essential. Geopolymer concrete (GPC) has emerged as a promising substitute, showing comparable or superior mechanical properties to PC composites<sup>2,3</sup>. GPC also characterizes benefits like high early-age strength<sup>4</sup>, recycling of industrial by-products<sup>4,5</sup>, reduced CO, emissions, improved energy efficiency<sup>3</sup>, and better thermal stability<sup>6,7</sup>. Unfortunately, GPC tends to be brittle, which can limit its ability to absorb and dissipate energy under stress, making it more susceptible to cracking and failure compared to PC concrete. To address this brittleness, previous studies demonstrated the integration of various fibers to enhance the ductility of GPC<sup>8,9</sup>. Previous studies<sup>8-10</sup> shows that GPCs, depending on fiber type and quantity, offer improved strength, deflection, toughness, and resistance to cracking, thermal exposure, and impact loads. Various types of fibers have been utilized for GPCs, including steel fibers<sup>11</sup>, synthetic fibers<sup>9,10</sup>, macro and microfibers<sup>12</sup>. Wang et al.<sup>13</sup> explored the fracture properties of the GPC with different basalt fiber (BF) percentages up to 0.15%, including fracture toughness, fracture energy, crack propagation length. It was revealed that the incorporation of BFs enhanced the peak load, fracture toughness, and fracture energy of the GPCs. Recent research revealed that the mechanical properties of concrete containing BFs has produced varying results regarding its compressive strength (CS)<sup>13–15</sup>. Branston et al. 16 and Zhang et al. 17 found that adding BFs at 0.31-2.0% by volume led to a significant reduction in CS, ranging from 31-45%. On the contrary, Sohail et al. 18 and Alnahhal et al. 19 observed a slight increase in CS by

<sup>1</sup>Department of Civil Engineering, Higher Future Institute of Engineering and Technology in Mansoura, Mansoura, Egypt. <sup>2</sup>Civil and Architectural Construction Department, Faculty of Technology and Education, Suez University, Suez, Egypt. <sup>3</sup>Institute of Construction and Architecture, Slovak Academy of Sciences, Dúbravsk'a Cesta 9, 845 03 Bratislava, Slovak Republic. <sup>4</sup>Department of Construction and Building Engineering, High Institute of Engineering, October 6 City, Egypt. <sup>™</sup>email: taher@savba.sk

6.2–17.5% with BFs additions of 0.25–1.0%. Zhang et al.<sup>20</sup> reported that BFs at 0.5–1.5% had minimal impact on CS and elastic modulus. Whilst, the inclusion of BFs improved flexural strength (FS) and splitting tensile strength (STS), also enhancing post-cracking performance and flexural toughness.

In general, GPCs require two essential components: precursor materials and an alkali-activating solution. Commonly used source materials include GGBS<sup>21</sup>, fly ash<sup>4</sup>, metakaolin<sup>22</sup>, and glass powder<sup>23</sup>. Moreover, recent research is exploring new potential precursors for GPC production, such as volcanic pumice, which has garnered attention from researchers<sup>24-26</sup>. Volcanic pumice, a natural construction material, is formed through the rapid cooling of molten lava. This process results in gas-filled foamy magma that quickly solidifies into an amorphous porous rock. Its vesicular structure makes pumice relatively easy to process. Comprising a high SiO<sub>2</sub> content, the amorphous structure of pumice lends itself to excellent pozzolanic properties when finely ground. Safari et al.<sup>27</sup> produced GPCs using volcanic pumice powder (VPP) with different alkali concentrations ranging from 8 to 18 M. The samples were cured at room temperature, 60 °C, 80 °C, and 100 °C for periods ranging from 24 to 120 h. The findings indicated that optimal FS and CS were achieved for mixes cured at 60 °C for 120 h. Furthermore, high-strength paste could be obtained at elevated curing temperatures with shorter curing durations. However, the gains in FS and CSs were comparatively lower when compared to lower temperatures and longer curing durations<sup>24-26</sup>. According to Tahwia et al.<sup>28</sup> and Safari et al.<sup>29</sup>, the geopolymer product form pumice exhibits suitable workability and adequate early CSs when activated by NaOH and Na,SiO3. However, to accelerate the polymerization reaction and increase the strength of pumice-based geopolymer, a high concentration alkaline solution and temperature curing are needed. The cost of producing geopolymers from pumice is increasing due in large part to these methods. Additionally, GPC typically exhibit lower resistance to efflorescence compared to traditional concrete, particularly when exposed to moisture or direct water contact. Efflorescence in GPCs is marked by white carbonate deposits on the surface, a result of free alkali ions migrating through the pore network and reacting with CO<sub>2</sub> and moisture from the environment. This phenomenon is driven by the high concentration of soluble alkali ions, such as Na\* and OH\*, which are susceptible to leaching due to concentration gradients. The occurrence of efflorescence can negatively impact the GPC's microstructure by disrupting the balance of aluminum and destabilizing the Al-O-Si bonds. This disruption impairs the aluminosilicate gel network by reducing the amounts of Q<sup>4</sup> (4Al) and Al species, thereby diminishing the material's mechanical strength<sup>30,31</sup>.

As mentioned above, the existing literature extensively explores various reinforcing fibers in GPC. However, there is currently no studies that systematically investigates the combined effects of BF as a reinforcing agent and VPP as a precursor in high-strength geopolymer concrete (HSGC). While previous studies have examined the mechanical properties of geopolymer composites, the impact of BF on enhancing strength and thermal stability, alongside the role of VPP in microstructural development and efflorescence resistance, remains unexplored. Thus, the current paper aims to bridge this gap by optimizing the synergistic effects of VPP and BF on HSGC performance. Employing response surface methodology (RSM), we optimize key factors influencing workability, dry density, and mechanical properties, such as CS, FS, and STSs. The use of central composite design (CCD) enables a detailed assessment of the interactions between VPP and BF, leading to the identification of optimal mixture parameters for enhancing HSGC characteristics. Furthermore, the study evaluates the influence of VPP and BF on efflorescence and high-temperature resistance, addressing critical durability aspects. Finally, microstructural and thermogravimetric analyses of optimized samples are conducted to validate their thermal stability and overall performance, offering novel insights into the practical application of BF- and VPP-based HSGC.

### Experimental program Materials

In the current investigation, the HSGC were prepared with GGBS, silica fume (SF), VPP, BF, river sand, crushed limestone, and tap water. The physio-chemical characteristics of precursors (GGBS, VPP, and SF) are presented in Table 1 as determined by XRF. The specific gravity of the GGBS and SF is 2.91 and 2.21, respectively, 70.35% of the GGBS particles passes through  $\approx$  a 152-µm sieve. The Blaine fineness of GGBS and silica fume were 413 and 17,500 m²/kg, respectively. The VPP used in this study was sourced from a quarry in Hurghada, Egypt, and was crushed in a laboratory crusher until it passed through a 63-µm sieve, as illustrated in Fig. 1a. The macro-and microstructure of the VPP is presented in Fig. 1b and c. The microstructure of VPP is characterized by a porous and vesicular texture, as observed through SEM imaging. The images reveal a complex network of interconnected voids and small cavities distributed throughout the material (Fig. 1d). Additionally, the X-ray diffraction pattern of the VPP, shown in Fig. 2, indicates that the material exhibits a predominantly crystalline structure, as evidenced by the presence of distinct diffraction peaks corresponding to quartz, calcium aluminum silicide, and other crystalline phases. However, the presence of a diffuse background hump suggests that a certain fraction of the material may still contain an amorphous phase<sup>32</sup>. The chemical oxides of the VPP is detailed in Table 1. According to the chemical composition, the VVP was rich silica materials which in line with

Oxides, (%) by wt	CaO	SiO <sub>2</sub>	Al <sub>2</sub> O <sub>3</sub>	Fe <sub>2</sub> O <sub>3</sub>	SO <sub>3</sub>	Na <sub>2</sub> O	K <sub>2</sub> O	MgO	P <sub>2</sub> O <sub>5</sub>	MnO	TiO <sub>2</sub>	Others	L.O.I. (%)
GGBS	33.25	35.37	19.36	1.8	0.18	0.24	1.04	8.69	-	-	-	0.07	2.98
SF	1.94	95.22	-	0.61	-	0.23	0.9	0.16	-	-	-	0.94	-
VPP	3.77	67.43	15.56	3.96	0.13	3.75	4.23	0.37	0.14	0.09	0.52	0.05	-

Table 1. Oxides of the used materials (wt., %) by XRF.



Fig. 1. Crushing machine, macro and micro-structure of used VPP.

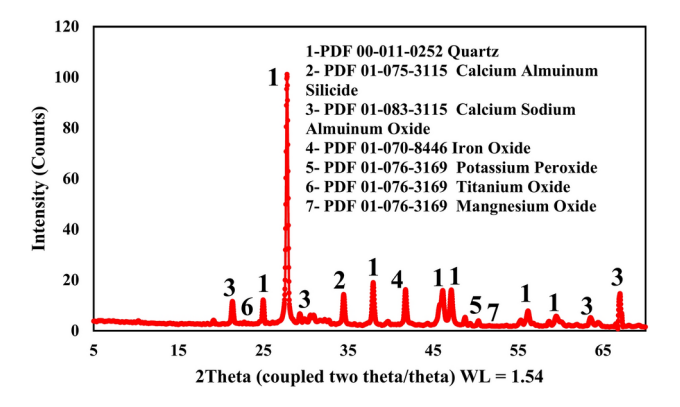


Fig. 2. XRD pattern of VPP.

previous studies. The particle size distribution (PSD) of the GGBS and VPP is illustrated in Fig. 3. It was found that the median particle diameter (D50) of the VPP, at 13.25  $\mu$ m, is smaller than that of the GGBS. 14M NaOH was dissolved in distilled water and mixed with Na<sub>2</sub>SiO<sub>3</sub> solution in ratio of 1:2.1 to prepare the alkali activation solution (AAS). Na<sub>2</sub>SiO<sub>3</sub> composition is 29.22% of SiO<sub>2</sub>, 13.66% of Na<sub>2</sub>O, and 57.12% of H<sub>2</sub>O (by mass) and density of 1.39 g/cm<sup>3</sup>.

The river sand (RS) employed in the current investigation with a size range of < 4.75 mm was used as fine aggregate. The water absorption rate of the used RS was 1.02%, and its fineness modulus was 3.03. The limestone had a maximum diameter of 12 mm, and its water absorption was 0.77% was used as a coarse aggregate. Basalt fiber (BF) was used as the reinforcing agent, with a length of 13 mm and a density of 2.56 g/cm³. The main physical and mechanical properties of BF are summarized in Table 2. BF exhibited a high tensile strength of 2000 MPa and an elastic modulus of 91 GPa, which indicates its potential to significantly enhance the mechanical performance of the concrete matrix. The macro and micro images of BF are presented in Fig. 4, where the fibers appear highly homogeneous with a predominantly smooth surface (Fig. 4b). Some fibers contained small particles and displayed a fairly smooth texture with irregular oval areas. The incorporation of BF in concrete is expected to improve its tensile strength, crack resistance, and durability due to the high mechanical properties of the fibers. The high elastic modulus and tensile strength contribute to better stress distribution and reinforcement

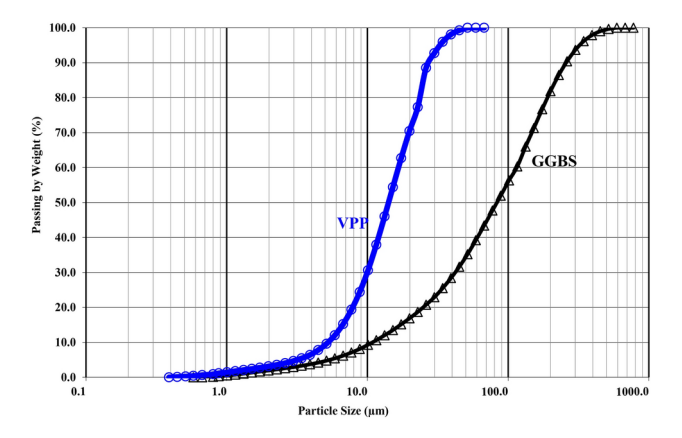


Fig. 3. PSD of used GGBS and VPP.

Length (mm)	Tensile strength (MPa)	Elastic modulus (GPa)	Density (g/cm <sup>3</sup> )	
13	2000	91	2.56	

**Table 2**. Main parameters of BF.

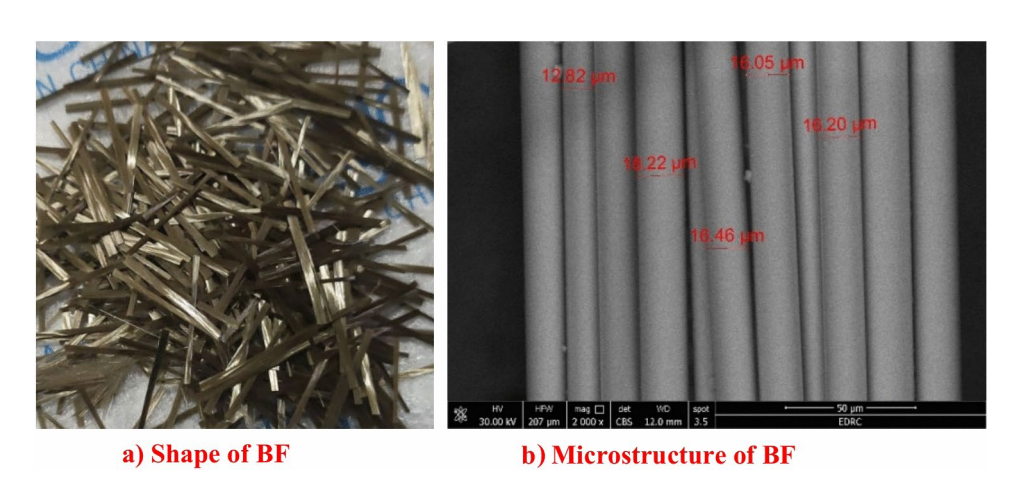


Fig. 4. Macro and micro-structure of used basalt fiber.

Mix ID		GPV0	GPV10	GPV20	GPV30	GPV40	GPF0.75	GPF1.0	GCF1.5
VPP	(%)	-	10	20	30	40	-	-	-
BF	(%)	-	0.5	0.5	0.5	0.5	0.75	1.0	1.5
GGBS	(Kg/m³)	417	375.3	333.6	291.9	250.2	417	417	417
SF	(Kg/m³)	106	106	106	106	106	106	106	106

**Table 3**. Mixture proportions of HSGCs.

efficiency within the cementitious matrix. Additionally, a polycarboxylate-based superplasticizer (SP) with 1.15 specific gravity was used, according to *ASTM C494 Type F*.

#### Preparation and optimization program

The experimental work was organized into two main sections. First, eight different mixtures were designed and prepared to investigate the combined effects of incorporating VPP and BF in the production of HSGC according to our previous studies<sup>5,28,32</sup>. In these mixtures, VPP was used as a partial replacement for GGBS at volumes ranging from 0 to 40%, while BF was added in quantities from 0.5 to 1.5% by volume. The mix proportions for these mixtures are detailed in Table 3. In the second part, seventeen trial mixes were designed

and evaluated experimentally using RSM. RSM was employed to optimize the variables with the goal of maximizing the workability, density, CS, FS, and STS of the HSGC samples. Two key factors, each with three levels, were considered for the HSGC mixtures: the replacement of VPP with 0%, 20%, and 40% by volume of GGBS, and varying BF contents of 0.5%, 0.75%, and 1.5% by mass of precursor material. The upper limits for VPP and BF were set at 40% and 1.5%, respectively, as detailed in Table 4. To evaluate the interaction of these parameters systematically, a CCD was employed. Each parameter was assessed at five levels ( $-\alpha$ , -1, 0, +1, and  $+\alpha$ ), covering factorial, axial, and central points. This approach resulted in a total of 17 experimental runs, as outlined in Table 4.

To prepare the HSGC samples, initially, the fine aggregate and limestone were introduced into the blender and mixed for 0.5 min. Subsequently, GGBS was blended separately with VPP and silica fume, and the resulting mixture was incorporated to the blender and mixed for 2 min. Following this, the alkali activation solution was gradually poured into the blender, with mixing continuing for an additional 2 min. After pouring the HSGC into moulds, the moulds were placed on a vibration table to enhance compaction and remove air bubbles. Based on our prior research, it found that curing geopolymers at elevated temperatures, particularly between 60 and 80 °C, proves to be one of the most effective methods<sup>33</sup>. Thus, the HSGC were cured in a hot-air furnace at 60 °C for 3 days before being stored at ambient curing until the testing day. The systematic process for producing, refining, and assessing HSGC is shown in Fig. 5.

#### Testing methods

To assess the workability of HSGC, the mixture was tested according to ASTM C143 using a slump cone test. The cone was placed on a level surface and filled with fresh HSGC in three equal layers, each rodded to consolidate. After leveling the top of the cone with the mixture, the cone was carefully lifted, allowing the sample to slump. The final height of the slumped sample was measured and subtracted from the original height of the cone to determine workability. CS of cubic samples (100 mm×100 mm×100 mm) was evaluated using a standard compression machine with a loading rate of 1.2 kN/s. Given that ambient-cured geopolymers typically increase in strength with age<sup>33</sup>, tests were conducted at 3, 7, 28, and 56 days to monitor the strength development of the HSGC. FS and STS were measured on prismatic (400 × 100 × 100 mm) and cylindrical (200 mm height × 100 mm diameter) samples, respectively, following ASTM C78 and ASTM C496 standards. The dry density of the mixtures was determined in accordance with ASTM C138/C138M. To evaluate high-temperature resistance, 28day cured HSGC samples were heated to 200, 400, 600, and 800 °C in a locally made electric furnace at 1 h, with a heating rate of 8 °C/minute. Samples were maintained at these temperatures for one hour and then allowed to cool naturally with the furnace door open. After cooling, residual CS was measured. Efflorescence was assessed by inspecting 50 mm × 50 mm × 100 mm samples for white crystallization. To simulate partially saturated conditions, samples cured for 56 days were submerged in water to a depth of 15 mm to 20 mm at 24 ± 3 °C and  $60 \pm 5\%$  relative humidity. The water level was regularly adjusted to prevent rapid absorption and evaporation.

For microstructural analysis, small pieces of HSGC samples were carefully cut using a thin diamond saw, then vacuum-coated with 10 nm of carbon to prevent charging during imaging. Samples were attached to a holder with carbon for scanning electron microscopy (SEM). Additionally, thermogravimetric analysis (TGA) and derivative thermogravimetry (DTG) were evaluated to investigate the thermal stability of the samples.

	VPP	BF	GGBS	SF	NaOH	Na <sub>2</sub> SiO <sub>3</sub>	Water	SP	RS	LS
Mix ID	(%)		(Kg/m³)							
FG1	20	0.75	333.6							
FG2	40	1.50	250.2							
FG3	20	0.75	333.6							
FG4	20	1.50	333.6							
FG5	0	1.50	417.0							
FG6	40	0.50	250.2							
FG7	0	1.50	417.0							
FG8	40	0.75	250.2	106	44	210	54	10.45	456	872
FG9	0	0.50	417.0							
FG10	0	0.75	417.0							
FG11	0	0.50	417.0							
FG12	20	0.75	333.6							
FG13	20	0.75	333.6							
FG14	20	0.50	333.6							
FG15	20	0.75	333.6							
FG16	40	1.50	250.2							
FG17	40	0.50	250.2							

**Table 4**. Mix quantites for one m<sup>3</sup> of HSGCs using RSM.

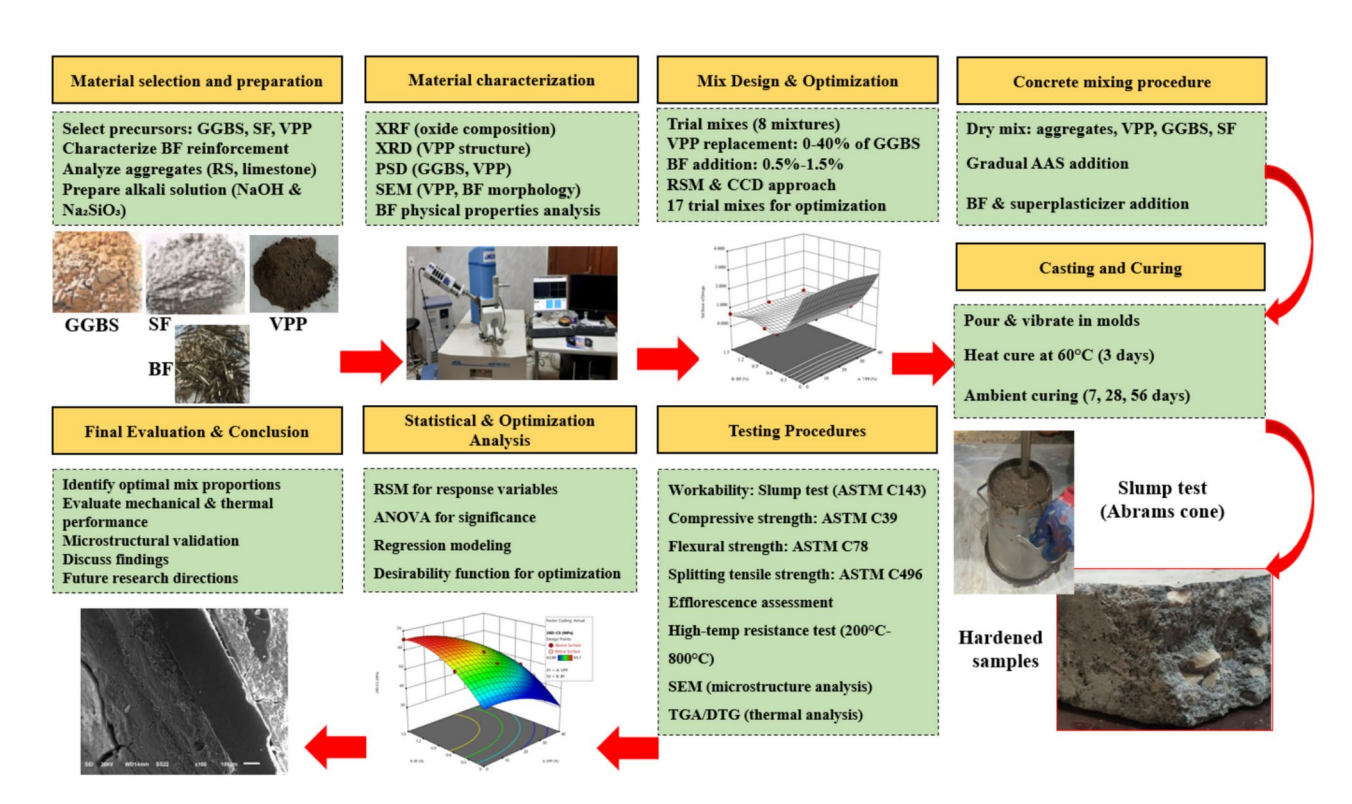


Fig. 5. Flow chart of the production of HSGC, optimization, and evaluation.

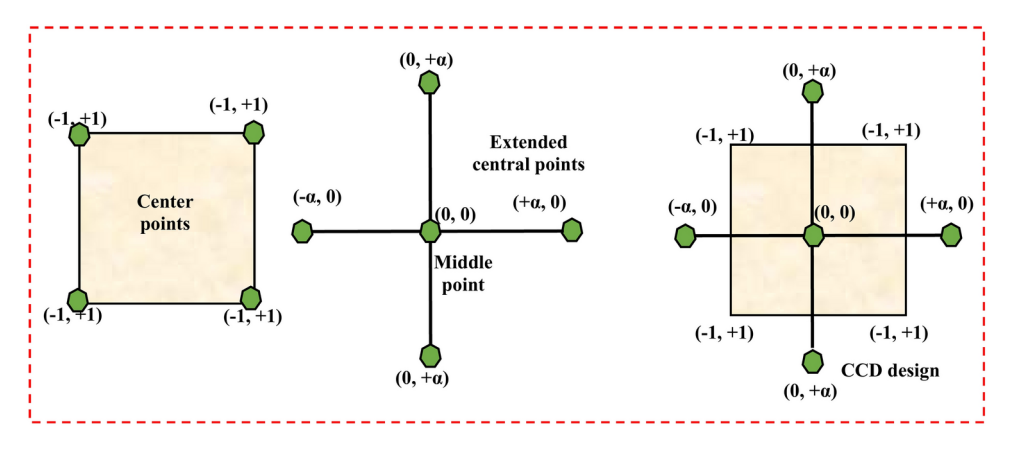


Fig. 6. CCD module.

#### Statistical analysis

RSM is a statistical technique used to establish and validate the relationships between input variables and out responses. The RSM process involves four primary steps: designing the experiment, collecting data through experimentation, developing a numerical model, and optimizing and validating the model<sup>34</sup>. CCD is a particularly effective and commonly used approach for experimental design within RSM<sup>35</sup>. As illustrated in Fig. 6, CCD typically involves a two-level factorial design. Data points are chosen based on several criteria: corner points representing all +1 and -1 design points, midpoints between all factors, and star points representing extreme combinations. For graphical analysis, ANOVA was utilized to clarify interactions between the input variables and outputs, aiming to forecast statistical factors. Regression-analysis was conducted on the tested results using *Design-Expert software*, which facilitated the visualization of response surfaces and contour plots under optimal conditions. This software also enabled the evaluation of statistical significance through F-tests. The polynomial accuracy model was evaluated using the coefficient of determination (R<sup>2</sup>). Key terms in the model were identified by analyzing P-values at a 95% confidence interval. *Design-Expert software* facilitated the experimental design and statistical modeling, using ANOVA to assess the significance of main factors, including linear, quadratic terms, and their interactions for fresh and mechanical properties. Significant terms were then used to formulate a regression-equation, as shown in Eq. (1).

$$y = \beta 0 + \sum \beta_i x_i + \sum \beta_{ii} x_i^2 + \sum \beta_{ij} x_i x_j$$
 (1)

where, the coefficients  $\beta_0$ ,  $\beta_i$ , and  $\beta_{ii}$  are obtained from the regression model, while  $x_i$  and  $x_j$  represent the independent variables.

In addition, the desirability function (DF) was used to identify the optimal factors of %VPP and BF for designing HSGC<sup>35</sup>. The objective was to maximize strength performance using Eq. (2). When the output fails to meet specification requirements, the desirability (denoted as d<sub>i</sub>) tends towards zero; conversely, when specifications are fulfilled, d<sub>i</sub> approaches 1.

Desirability = 
$$(\mathbf{d}_1^{\mathrm{r1}} \times \mathbf{d}_2^{\mathrm{r2}} \times \mathbf{d}_3^{\mathrm{r3}} \times \ldots \times \mathbf{d}_n^{\mathrm{rn}})^{1/\sum ri} = \left[\int_{i=1}^n \mathbf{d}_n^{\mathrm{rn}}\right]^{1/\sum ri}$$
 (2)

where, 'n' represents the number of input parameters and responses involved in the optimization. The term 'ri' denotes the relative importance of each variable or response, ranging between 1+ and 5+, with lower to higher importance levels.

## Results and discussion Impact of BF on the mechanical performance

The CS of HSGC with BFs at 3, 7, 28, and 56 days is presented in Fig. 7a. As shown, the samples containing BFs exhibit higher CS compared to the control mixture (GPV0) at all ages. Specifically, as the BF content increases, the CS of the HSGCs rises, with increases of 6.81%, 12.91%, and 13.59% for additions of 0.75%, 1.0%, and 1.5% BF at 7 days, respectively, compared to the GPV0. Additionally, the inclusion of BFs results in higher strength mixtures, reaching 61.77 MPa, 63.11 MPa, and 65.70 MPa at 28 days with 0.75%, 1.0%, and 1.5% BF, respectively. These values represent CS increases of 7.67%, 10.0%, and 14.51% over the GPV0, respectively. Also, HSGC mixtures exhibit a notable increase in strength as time progresses. For instance, the HSGC containing 1.5% BF shows enhancements in CS of 73.2% (51.54 MPa), 120.8% (65.70 MPa), and 138.8% (71.05 MPa) at 7, 28, and 56 days, respectively, compared to the strength at 3 days. This enhancement is primarily attributed to ongoing chemical reactions between the precursor and the alkaline activator 17,25. As the geopolymer matrix matures, additional crystalline and gel-like phases continue to form, leading to increased densification of the material structure. This ongoing reaction enhances the strength of the geopolymer matrix. Specifically, the presence of Si and Al ions in the raw materials (see Table 1), which are readily leached by NaOH, facilitates the formation of C-A-S-H and N-A-S-H gels. Furthermore, the calcium found in GGBS plays a significant role in promoting the

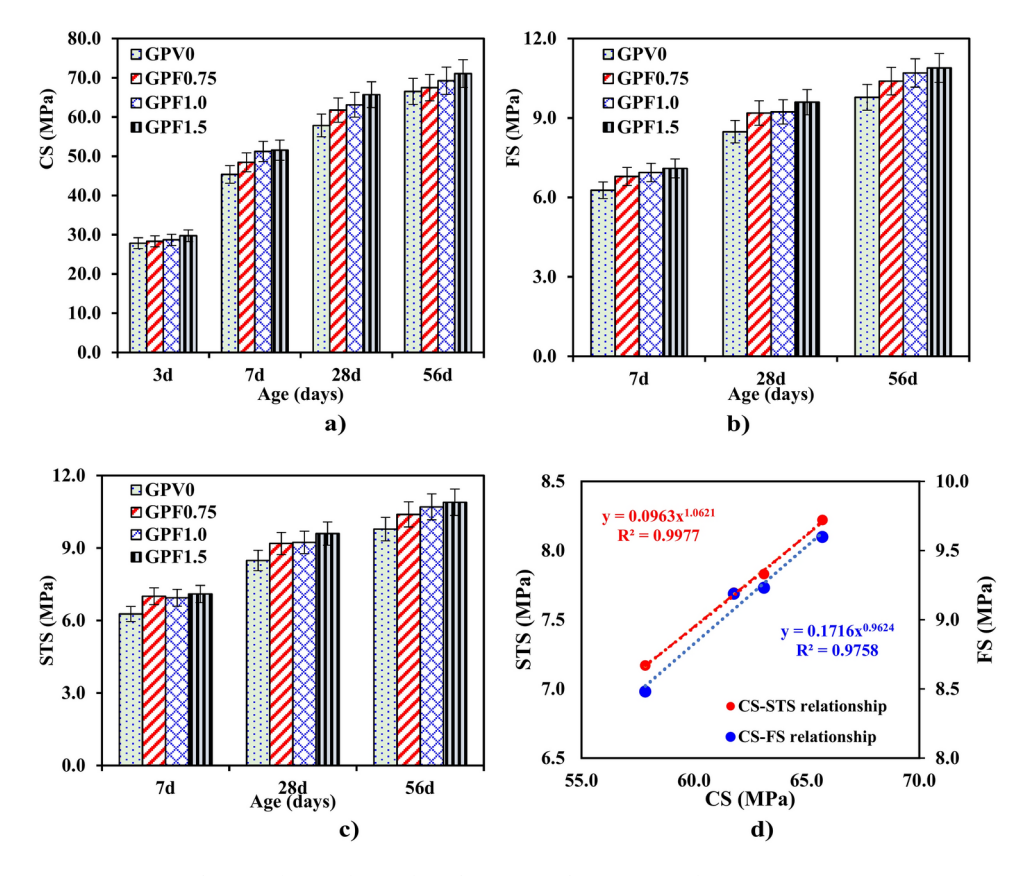


Fig. 7. Impact of BF on the mechanical performance of HSGC samples.

setting and hardening of the geopolymer matrix, with C-A-S-H and N-A-S-H being the primary contributors to strength development <sup>13,17</sup>. Moreover, the random distribution of BFs creates a bridging effect that helps mitigate the rapid spread of cracks, thereby enhancing the strength of the HSGC<sup>16,17</sup>.

Figure 7b and c illustrate the FS and STS results for HSGC containing BFs. At 7 days, the FSs for the samples with varying BF contents were GPV0 (6.27 MPa), GPF0.75 (6.79 MPa), GPF1.0 (6.94 MPa), and GPF1.5 (7.10 MPa). At 28 days, these strengths improved to 8.48 MPa, 9.19 MPa, 9.23 MPa, and 9.60 MPa, respectively. The inclusion of BFs led to FS increases of 8.33%, 8.84%, and 13.17% for 0.75%, 1.0%, and 1.5% BF content compared to the GPV0 at 28 days. Similarly, at 7 days, the STSs for the HSGC were GPV0 (5.24 MPa), GPF0.75 (5.63 MPa), GPF1.0 (5.77 MPa), and GPF1.5 (6.01 MPa), rising to 7.17 MPa, 7.70 MPa, 7.83 MPa, and 8.22 MPa at 28 days. This represented increase of 7.34%, 9.21%, and 14.46% in STS for 0.75%, 1.0%, and 1.5% BF content compared to the GPV0 at 28 days. In this context, Almohammed et al.<sup>36</sup> demonstrated that increasing BF content led to improved mechanical properties, with the highest FS of 5.11 MPa at 0.4% fiber volume and the highest STS of 2.24 MPa at 0.3% fiber volume. Zhang and Wang<sup>37</sup> and Huang<sup>38</sup> identified an optimal fiber content range of 0.2%-0.3% for improving flexural strength. However, Katkhuda and Shatarat<sup>39</sup> reported that a fiber content of 1.5% yielded the highest flexural strength, with an increase of 61.45% compared to fiber-free samples. Similarly, Alnahhal<sup>40</sup> observed a progressive enhancement in flexural strength, ranging from 37 to 42%, as fiber content increased from 0.5 to 1.5%. Both FS and STSs showed a positive correlation with fiber content, with 1.5% BF showing the most significant improvement. A regression-analysis was carried out to examine the relationships between the CS, STS, and FSs of HSGC using experimental data (Fig. 7d). The analysis showed a considerable power-correlation between CS and FS, with a highly significant correlation coefficient of R<sup>2</sup>=0.9758. Additionally, the relationship between CS and STS was also highly significant, with a correlation coefficient of  $R^2 = 0.9977$ .

#### Impact of VPP on the mechanical performance

The effect of VPP content on mechanical performance of HSGC is illustrated in Fig. 8. The results indicate that increasing the proportion of VPP in GGBS-based HSGC typically leads to a reduction in CS, regardless of curing conditions or sample age. These findings align with the studies by<sup>24,27,30</sup>, which found that higher GGBS content in the GGBS/natural pozzolan geopolymer matrix enhances CS due to the high heat of hydration associated with GGBS (Fig. 8a). Ismail et al. reported that the alkali activation of GGBS primarily results in the formation of C-S-H and/or C-A-S-H gels, similar to those observed in Portland cement<sup>41</sup>. The increased strength in samples with more GGBS is likely due to the formation of these gel phases, which contribute to a denser microstructure<sup>7,21</sup>. At 7 days, the average CSs were 45.37 MPa for GPV0, 44.22 MPa for GPV10, 42.82 MPa for GPV20, 38.27 MPa for GPV30, and 34.93 MPa for GPV40. The HSGC with 40% VPP showed a 23% reduction in CS compared to

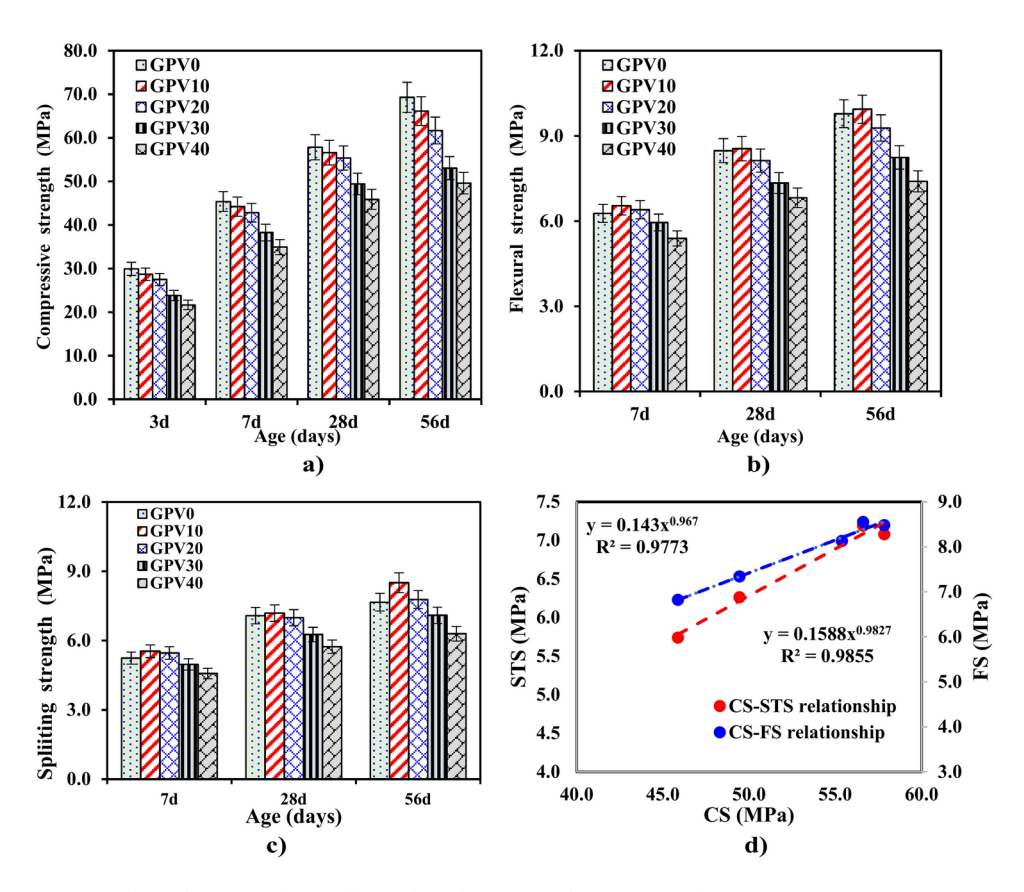


Fig. 8. Effect of VPP on the mechanical performance of HSGC samples.

GPV0. By 28 days, the CSs for GPV0, GPV10, GPV20, GPV30, and GPV40 increased to 57.84 MPa, 56.61 MPa, 55.38 MPa, 49.44 MPa, and 45.87 MPa, respectively. In contrast, the addition of VPP improved FS and STSs. At 28 days, the average FS (Fig. 8b) and STS (Fig. 8c) were 8.48 MPa and 7.08 MPa for GPV0, 8.55 MPa and 7.19 MPa for GPV10, 8.13 MPa and 6.99 MPa for GPV20, 7.37 MPa and 6.26 MPa for GPV30, and 6.82 MPa and 5.74 MPa for GPV40. Notably, the GPV10 mixture showed a 0.82% increase in FS and a 1.57% increase in STS compared to the GPV0. A regression-analysis was also performed to explore the relationships among the CS, STS, and FSs of HSGC based on experimental data (Fig. 8d). The result confirmed a significant power correlation between CS and FS, with a highly significant correlation coefficient of R<sup>2</sup>=0.9855. Similarly, the relationship between CS and STS was also highly significant, with a correlation coefficient of R<sup>2</sup>=0.9773. The incorporation of VPP has a notable impact on the interaction between coarse aggregate and the geopolymer matrix, particularly within the internal interfacial transition zone (ITZ), as depicted in Fig. 9. Specifically, Fig. 9e illustrates that the presence of VPP can lead to a less dense and potentially weaker ITZ, attributed to an increased volume of voids and a reduction in matrix density. This phenomenon will be further elaborated in the microstructural analysis.

#### **Efflorescence of HSGC**

The schematic diagram illustrating the efflorescence mechanism in HSGC is shown in Fig. 10. In this process, an excess alkali activation solution within the geopolymer matrix moves to the HSGC surface due to evaporation, where it reacts with CO, from the air to form carbonates. Although geopolymerization can quickly consume alkali species at early ages, there remains a significant risk of efflorescence due to the substantial amount of residual alkali in the pore solution. When Na,SiO<sub>3</sub> and NaOH are employed to synthesis the geopolymer, Na<sup>+</sup>, OH-, and various silicate structures can migrate to the HSGC surface. Efflorescence is influenced not only by the geopolymer's structure but also by its preparation conditions and the external environment<sup>42</sup>. To effectively inhibit efflorescence, it is essential to focus on enhancing the geopolymer's properties. A well-structured geopolymer with low porosity and small pore sizes can significantly reduce alkali solution migration by densifying its structure. Figure 11 illustrates the white crystals formed by efflorescence on HSGC samples exposed to water. The HSGC with higher BF content exhibit a less pronounced degree of white crystalline formation, which related to the enhanced microstructure as discussed later. (Fig. 11). In other words, efflorescence causes visible whitish deposits on the surface of the HSGC and may lead to surface degradation<sup>30,43</sup>. The GPV0 shows a significantly larger area and thickness of white crystals compared to the GPF1.5 mixture, reflecting an improved microstructure of the matrix. The extent of efflorescence on HSGC with varying VPP contents is also presented in Fig. 12. The area and thickness of the white crystals increase significantly with the addition of VPP, indicating that VPP accelerates efflorescence formation. Finally, compared to the control mix, the GPV10 sample shows a significant reduction in both the area and thickness of the white crystals, while the GPV40 sample exhibits an increase in efflorescence. Karaaslan et al. 42 further show that alkali migration and carbonation cause efflorescence in geopolymer bindings. The present work emphasizes the influence of VPP and BF on HSGC performance, whereas Karaaslan et al. stress the function of heat curing and GPC in lowering efflorescence. Finally, the current

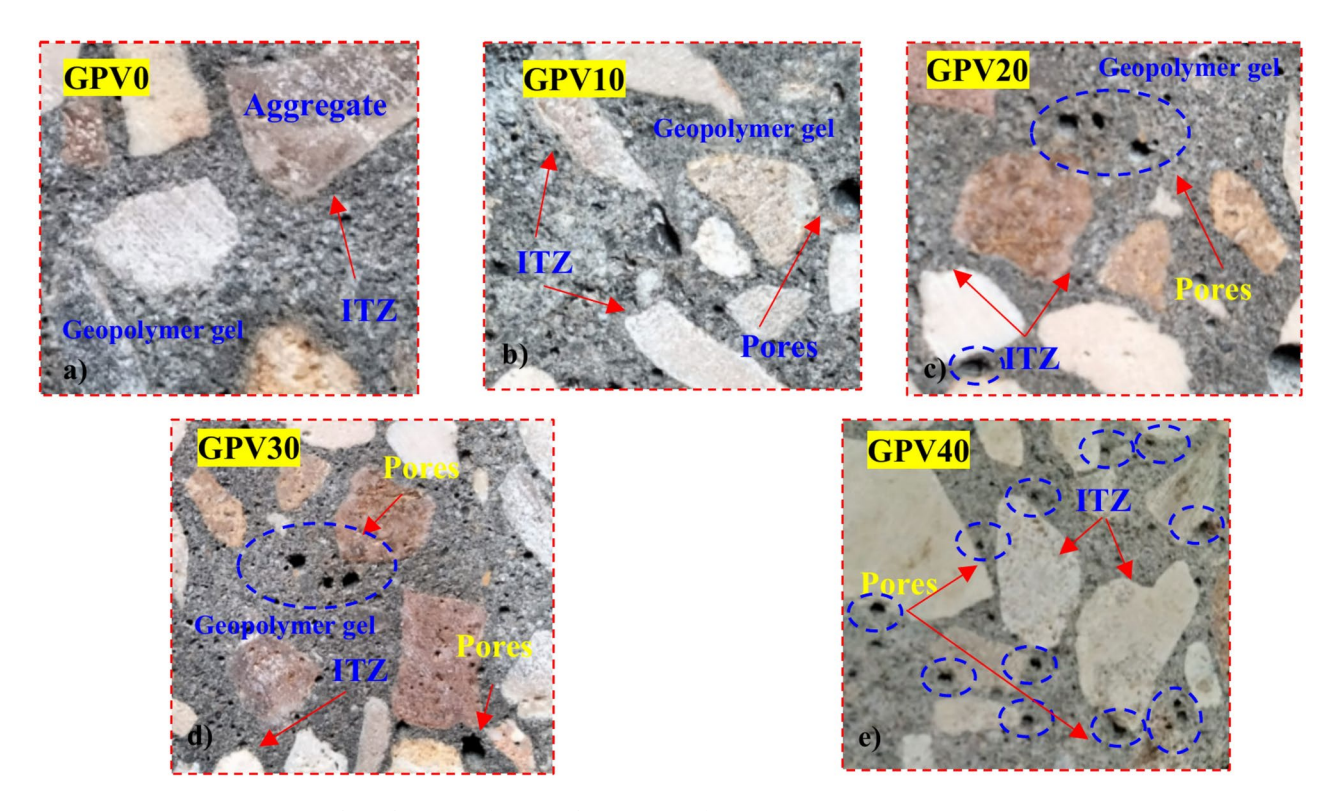


Fig. 9. Effect of VPP on the ITZ of HSGC samples.

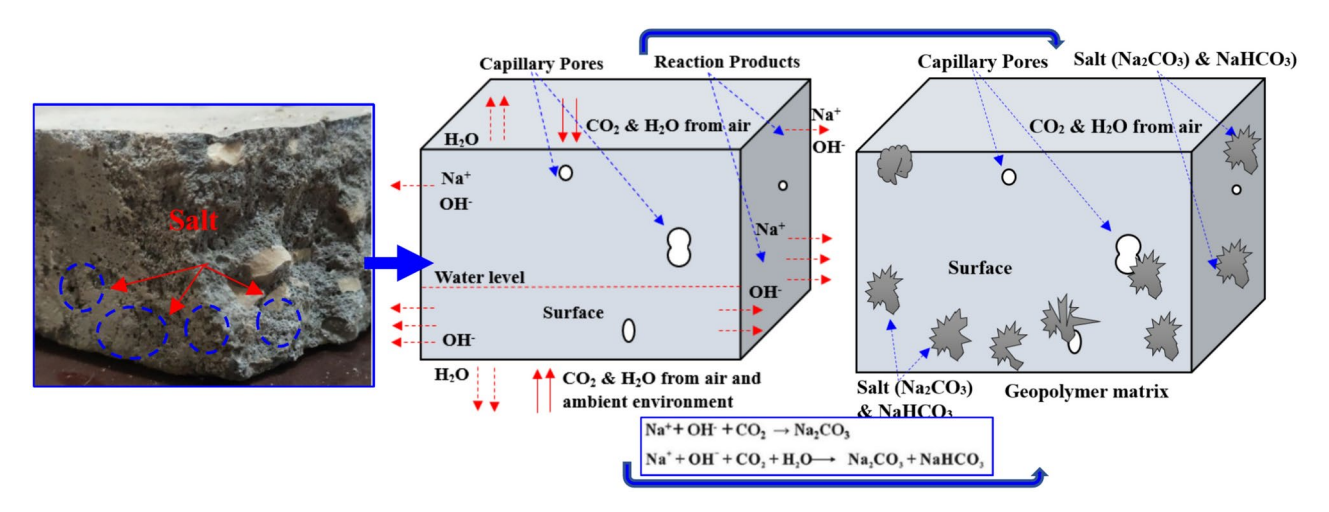


Fig. 10. Schematic diagram of the HSGC efflorescence mechanism.

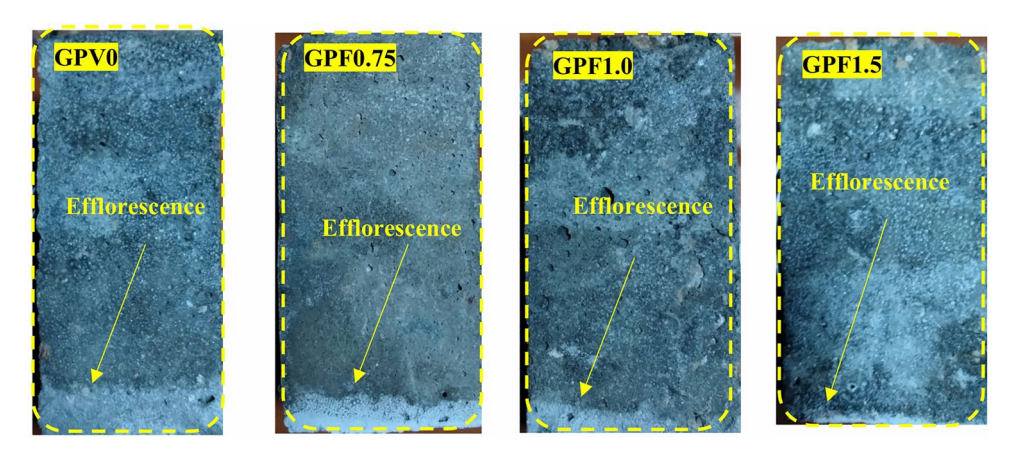


Fig. 11. Effect of BF on the efflorescence of HSGC samples.

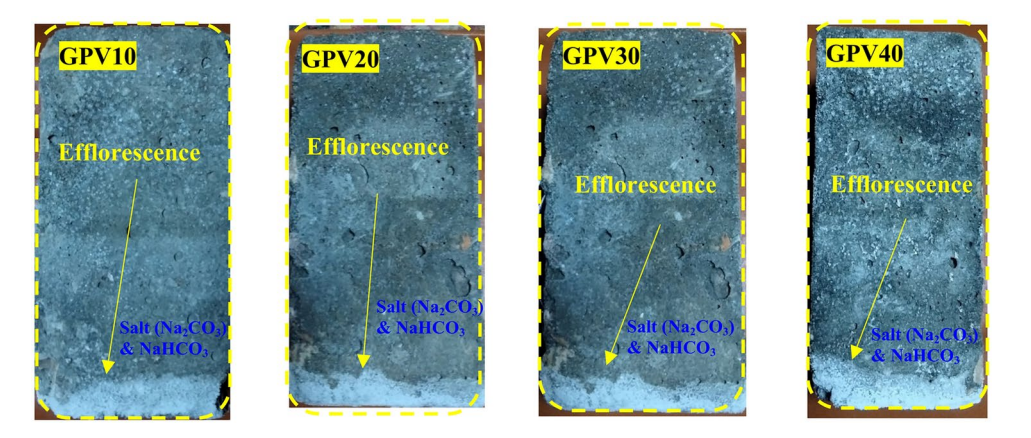


Fig. 12. Effect of VPP on the efflorescence of HSGC samples.

results show that while adequate BF content improves compactness and reduces efflorescence, excessive VPP increases efflorescence.

#### Optimum mix design

Modelling and statistical evaluation

The test results for the mechanical strengths and dry density of HSGC samples with varying percentages of VPP and BF are summarized in Table 5. The findings reveal that the inclusion of BF significantly improves the strength of HSGC, while VPP inclusion decreases both mechanical properties and dry density. Specifically, the CS, STS, and FS at 28 days achieved up to 65.70 MPa, 8.22 MPa, and 9.60 MPa, respectively. The dry density of the samples reached up to 1978 kg/m³. In this phase of the investigation, RSM was employed for optimization based on the above tested results. The aim was to define the optimal levels of VPP and BF to maximize workability, CS, FS, and STS, while minimizing dry density. Non-linear fitting of different models was carried out using model summary statistics, the sum of squares of deviation, and fitting errors. Quadratic polynomial models were developed by estimating parameter coefficients through multiple regression analyses. The polynomial regression models for all responses are detailed in Eqs. (3)–(7).

Workability = 
$$179.7158 + 1.1584 \text{ VPP } - 164.620 \text{BF } - 0.1416 \text{VPP} * \text{BF } - 0.0217 \text{VPP}^2 + 63.5270 \text{BF}^2$$
 (3)

Dry density 
$$= 2051.2786 - 1.750 \text{VPP} - 3.58933 \text{BF}$$
 (4)

$$28d - CS = 44.5938 + 0.1206VPP + 32.7484BF - 0.0445VPP * BF - 0.0117VPP^2 - 12.525BF^2$$
 (5)

$$28d - FS = 7.5768 + 0.0209VPP + 2.6623BF - 0.0165VPP * BF - 0.0017VPP^2 - 0.8234BF^2$$
 (6)

$$28d - STS = 5.6876 + 0.0347VPP + 3.550BF - 0.0056VPP * BF - 0.0019VPP^2 - 1.2264BF^2$$
 (7)

To ensure the accuracy and reliability of each regression analysis, several statistical metrics, including p-values, lack-of-fit assessments, and R<sup>2</sup> results, were calculated. The model terms, ANOVA results for each output, and descriptive statistics for each model are presented in Table 6. All output models and individual parameters are statistically significant at the 95% confidence level, as indicated by p-values less than 0.05. A significant effect on a response variable is confirmed by a high F-value and a p-value ≤0.05<sup>1,34</sup>. In this study, the F-values for CS and STS are 2799.1 and 881.75, respectively, both of which are highly significant with p-values < 0.0001. These high F-values suggest strong evidence that the independent variables (VPP and BF) have a substantial impact on the properties of HSGC. Additionally, the R2 values for workability, dry density, CS, FS, and STS are 93.7%, 92.9%, 99.8%, 99.7%, and 90.4%, respectively. An R<sup>2</sup> value close to 1 indicates a strong correlation between actual and predicted results, enhancing model precision. The variance between the predicted R<sup>2</sup> and adjusted R<sup>2</sup> for all output models is less than 0.2, confirming that the models are both reliable and well-fitted. The coefficient of variation (CV%) values for workability, dry density, CS, FS, and STS are 5.15, 0.405, 0.4357, 0.794, and 5.404, respectively, demonstrating the robustness of the constructed models. These findings support the models' great predictive power, especially for CS and STS, while workability, dry density, and FS show somewhat lower accuracy. However, the models are dependable for forecasting the mechanical and physical characteristics of HSGC mixtures, as evidenced by the high R<sup>2</sup> values and low standard deviations.

Figure 13 offers a comprehensive statistical analysis of the models with a scatter plot of expected versus actual values for each of the objective properties: workability, dry density, CS, FS, and STS. Data points in the scatter plot have strong prediction accuracy because they nearly overlap with the diagonal line. The findings

	Factor 1	Factor 2	R 1	R2	R3	R4	R5
	A: VPP	B:BF	Workability	28D-CS	28D-STS	28D-FS	28D-Density
Mix ID	%	%	mm	MPa	MPa	MPa	kg/m <sup>3</sup>
FG1	20	0.75	105	59.23	7.48	8.78	2013
FG2	40	1.5	79	49.06	6.19	6.60	1984
FG3	20	0.75	105	59.23	7.48	7.36	2013
FG4	20	1.5	88	61.35	8.15	9.47	1984
FG5	0	1.5	74	65.70	8.22	9.60	2051
FG6	40	0.5	127	42.89	5.36	6.38	1978
FG7	0	1.5	74	65.70	8.22	9.60	2051
FG8	40	0.75	88	46.88	5.87	6.97	1981
FG9	0	0.5	111	57.84	7.17	8.78	2051
FG10	0	0.75	100	61.77	7.70	9.19	2051
FG11	0	0.5	111	57.84	7.17	8.78	2051
FG12	20	0.75	105	59.23	7.48	8.78	2013
FG13	20	0.75	105	59.23	7.48	8.78	2013
FG14	20	0.5	121	55.38	6.99	8.13	2013
FG15	20	0.75	105	59.23	7.48	8.78	2013
FG16	40	1.5	80	49.06	6.19	6.60	1984
FG17	40	0.5	127	42.89	5.36	6.38	1978

Table 5. Response surface test results of HSGCs.

	Responses									
Models	Workability	Dry density	CS	STS	FS					
p-value	< 0.0001	< 0.0001	< 0.0001	< 0.0001	< 0.0001					
F-value	33.25	92.33	2799.1	881.75	20.84					
R <sup>2</sup>	0.937	0.929	0.998	0.997	0.904					
Adjusted R <sup>2</sup>	0.909	0.919	0.998	0.996	0.861					
Predicted R <sup>2</sup>	0.813	0.886	0.997	0.992	0.826					
Adequate precision	16.471	21.476	155.396	86.933	12.653					
Std. deviation	5.173	8.156	0.243	0.056	0.441					
Mean	100.294	2013.059	56.03	7.058	8.174					
C.V (%)	5.158	0.405	0.4357	0.794	5.404					

Table 6. Results of tested models.

demonstrate how effectively the models predict CS (Fig. 13c) and STS (Fig. 13), whereas the predictions for the remaining targets exhibit somewhat lower accuracy but are still appropriate for the dataset.

Based on the RSM modeling approach, Fig. 14 shows how the VPP content and BF dosage affect workability, dry density, CS, FS, and STS. The inverse relationship between BF content and flowability is displayed in Fig. 14a, where workability steadily declines as the BF replacement percentage in the geopolymer matrix rises from 0 to 1.5%. Furthermore, the image highlights how VPP affects workability. Likewise, Fig. 14b shows a steady decrease in dry density from 0 to 40% as VPP substitution increases. This decrease is explained by the fact that VPP has a lower specific gravity than GGBS, which lowers the geopolymer matrix's total density. The impact of VPP and BF content on strength attributes is further demonstrated in Fig. 14c, d, and e. As VPP replacement approaches 40% and replaces a sizable amount of GGBS, a discernible decrease in CS, FS, and STS is seen. The relationship between BF content and strength is nonlinear, though; CS, FS, and STS first rise with BF dosage, reaching a peak of 1.5% before falling. Before excessive fiber content results in decreased workability and possible microstructural discontinuities as proved in previous studies<sup>32,44,45</sup>, this peak represents an ideal fiber content that improves the mechanical performance of the geopolymer matrix. Ziada et al. 45 showed that adding BF to fly ash-based geopolymer considerably increased CS after 28 days, confirming this trend and proving a link between BF dosage and mechanical performance. BF's function in strengthening the structural integrity of geopolymer samples was further supported by the fact that its addition significantly increased FS.

#### Validation of ANOVA models

RSM was used to explore the interactions and effects of various factors on HSGC performance and to establish relationships between inputs and their outputs. Optimal results for VPP content and BF dosage were evaluated through a computational multi-objective optimization approach, employing a RSM and the DF<sup>34</sup>. The objective was to maximize workability, CS, STS, and FS while minimizing dry density, with all responses given equal importance. The DF appoints a value between 0 (an unsatisfactory response) and 1 (the optimal outcome) to a solution. Optimization objectives and benchmark criteria are outlined in Table 7. Using RSM, optimal ratios were identified as 17.79% VPP content and 0.69 BF dosage, resulting in a desirability function value of 0.643, which indicates a high level of reliability. Table 8 shows the numerical optimization results and highlights that the predicted error for the optimal HSGC proportions is under 5%, demonstrating the model's accuracy. Predicted values from individual response models were compared with experimental results, with Table 8 indicating a maximum deviation of 3.30% for CS, well below the 5% threshold and confirming high model precision to validate. Additionally, the test results of the optimal mixture were within the response range considered during optimization. It can be difficult to get the best value for every response in the same area. Consequently, the best way to find a solution that satisfies every response criterion is through multi-objective optimization. Following the creation and validation of ANOVA models, a global desirability function [Eq. (2)] was used for optimization. VPP and BF content were taken into consideration for optimizing the following five responses: workability, dry density, CS, STS, and FS. While the desire function (D.) varied from 0 (undesirable) to 1 (ideal), each response was given an importance rating on a scale of 1 to 5. The geometric mean of each desirability value was used to get the total desirability. While other parameters stayed within range, workability, CS, STS, and FS were optimized and the dry density was minimized in this study. Figure 15 provides a visual representation of the optimized HSGC and related reactions, Figure 16 displays the eco-efficient solution's overall desirability as well as the pertinent desirability of its variables and responses based on Eq. (2). In addition to the combined desirability function of 0.643 for the model, it is evident that the suggested model yields individual desirability values for VPP, BF, workability, dry density, CS, STS, and FS that correspond to 1, 1, 0.63, 0.45, 0.72, 0.75, and 0.70, respectively.

#### Microstructural analysis at ambient curing

Figure 17 presents SEM images of the optimized mixture prepared HSGC mixtures, as shown in Tables 6 and 8. To asses the effect of BF, Fig. 17 present SEM images of HSGC with BF at 28 days, demonstrating the interaction between the geopolymer matrix and the BF surface. The images indicate that the incorporation of BFs led to a denser and more homogeneous structure. The presence of calcium ions (Ca<sup>2+</sup>), along with the increased BF content, resulted in the formation of C-A-S-H and N-A-S-H, which is the primary reason for the denser

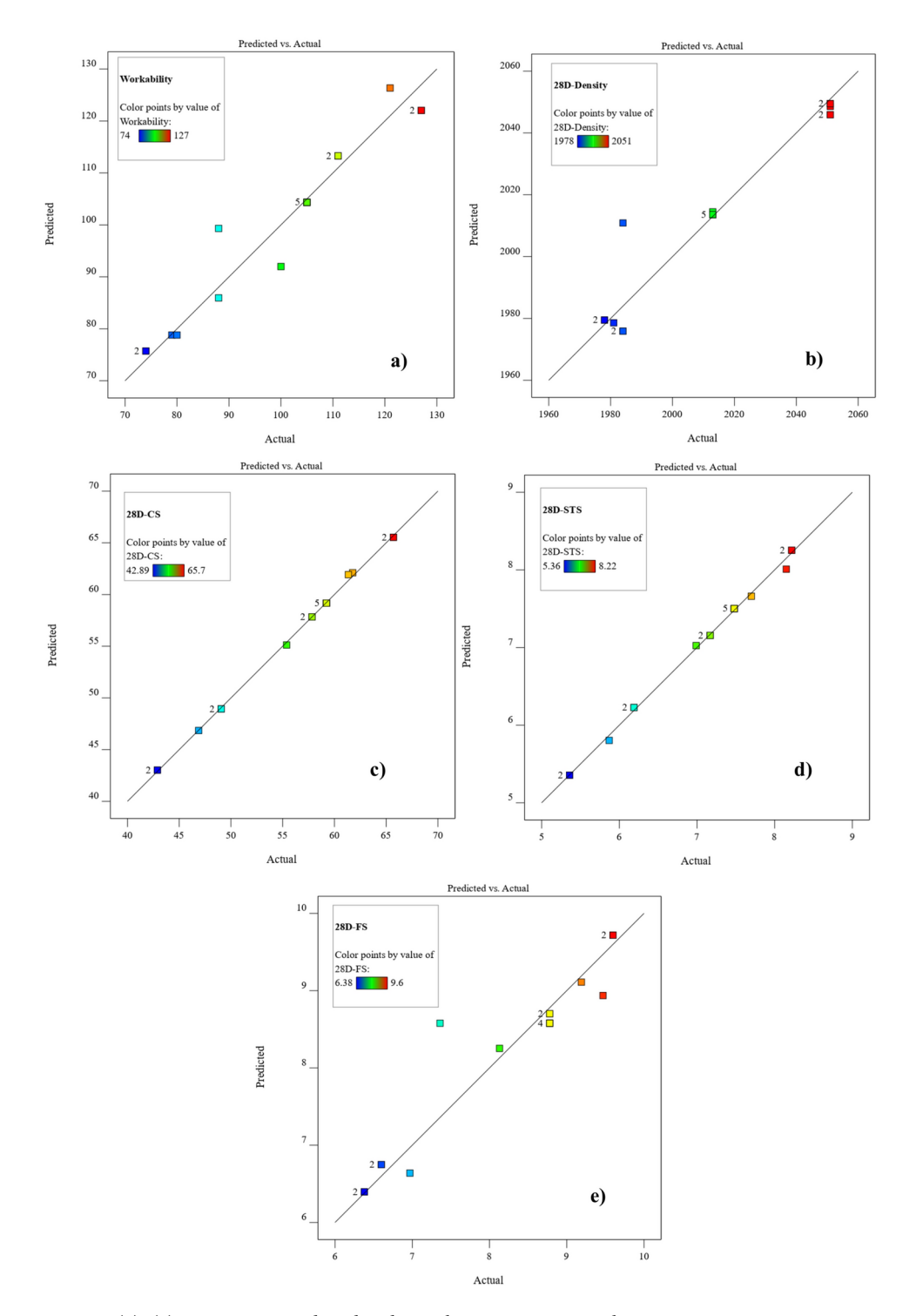


Fig. 13. (a)–(e) Comparing predicted and actual HSGC response values.

structure of FG5 (Figs. 17d) compared to the lower BF content in FG9 (Fig. 17g) and FG10 (Fig. 17h). In this context, Walkley et al. demonstrated that alkali-activated pastes containing C-(N)-A-S-H and N-A-S-H gels can be synthesized using high-purity calcium aluminosilicate powders. These powders, similar to GGBS but without minor impurities, influence gel properties based on composition. Higher calcium content promotes low-Al, high-Ca C-(N)-A-S-H formation with reduced AFm phases, while increased aluminum enhances Al inclusion, AFm phase formation, and additional N-A-S-H gel development. Additionally, they reported that small precursor variations significantly impact phase evolution, nanostructure, and mechanical properties<sup>46</sup>. In the geopolymer matrix, BFs act as micro-aggregates, enhancing CS. This dense structure contributes to the improved performance of HSGC<sup>47</sup>. Additionally, the optimized mixture (Fig. 17i) and FG5 (Fig. 17d) samples exhibit a strong and uniform bond between the geopolymer matrix, aggregate and fiber surface at the ITZ. In

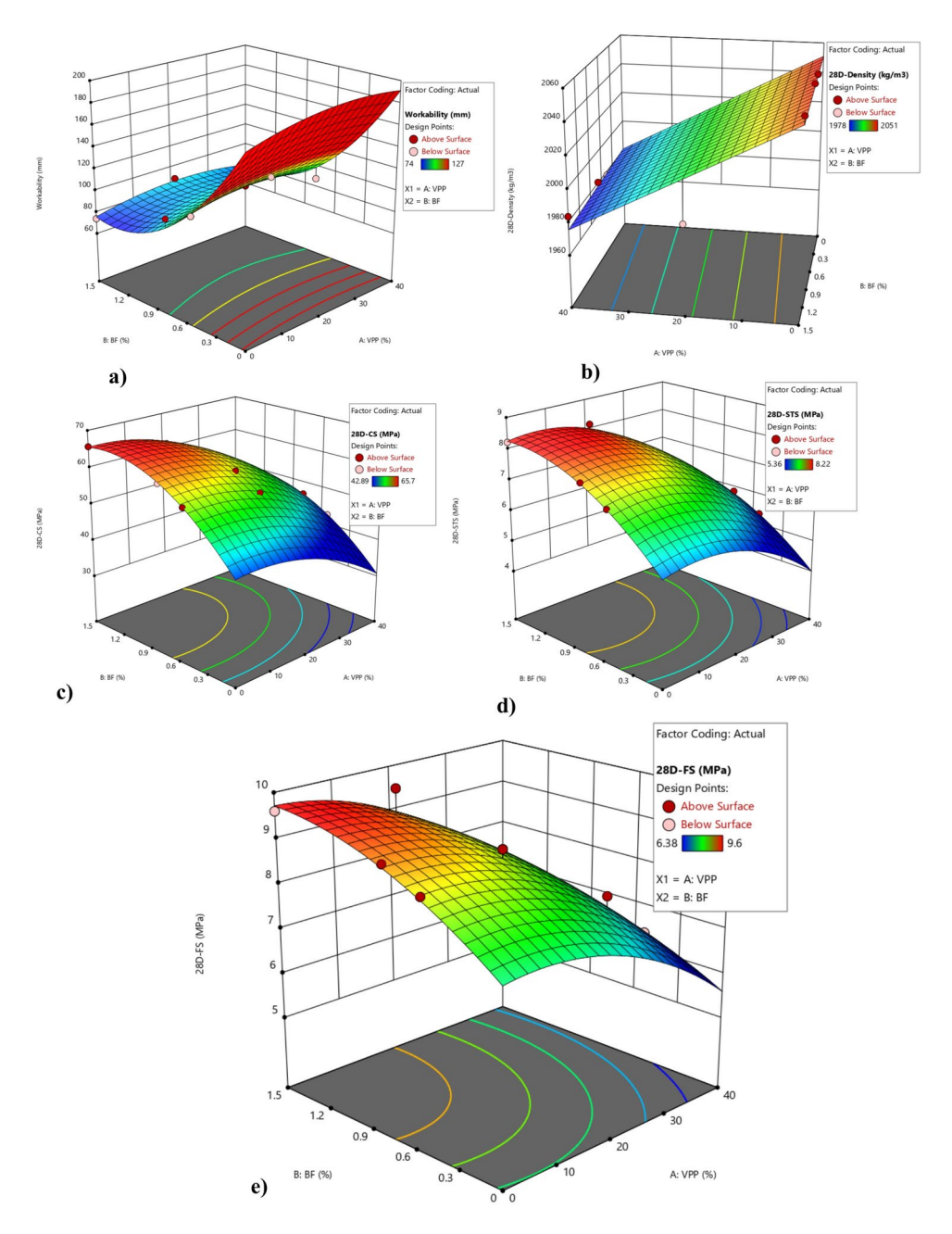


Fig. 14. Response surface plots for HSGC mixture analysis.

Input factors and output	Target	Lower	Upper
A: VPP (%)	In-range	0	40
B: BF (%)	In-range	0.50	1.5
Workability	Maximize	74	127
Dry density	Minimize	1978	2051
CS	Maximize	42.89	65.70
FS	Maximize	6.38	9.60
STS	Maximize	5.36	8.22

Table 7. Optimization objectives and benchmark criteria.

Responses	A: VPP (%)	B: BF (%)	Pred. value	Actu. value	Error (%)
Workability (mm)			107.5	103.0	4.03
Density (kg/m³)			2012.21	1981.88	1.77
CS (MPa)	17.79	0.69	59.25	61.21	3.30
FS (MPa)			8.64	7.88	8.70
STS (MPa)			7.51	6.23	17.04

**Table 8**. Verification of optimal mixture model.

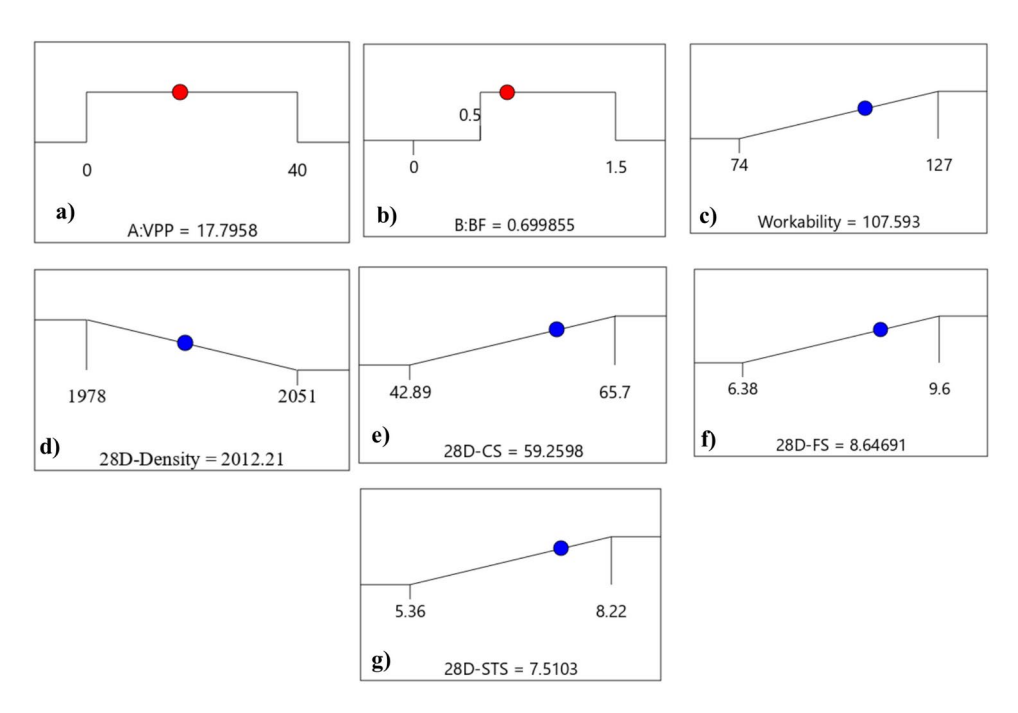


Fig. 15. Ramps of optimized HSGC.

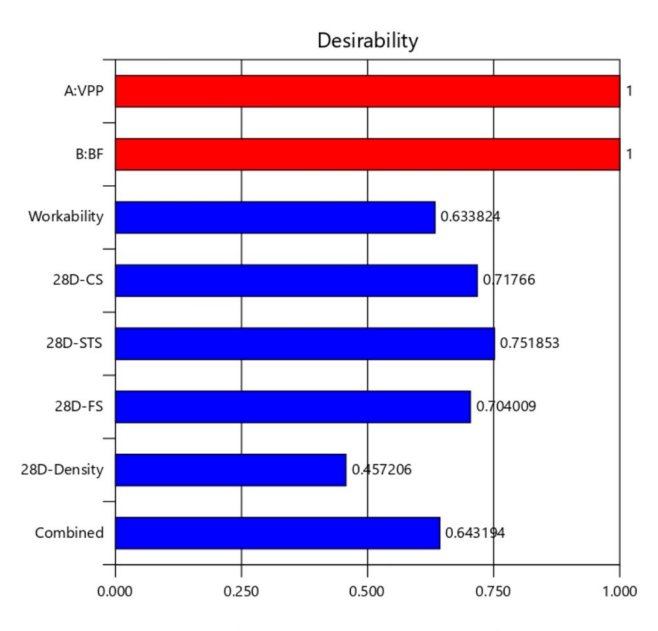


Fig. 16. Desirability of proposed HSGC mixture for its individual variables and their combination.

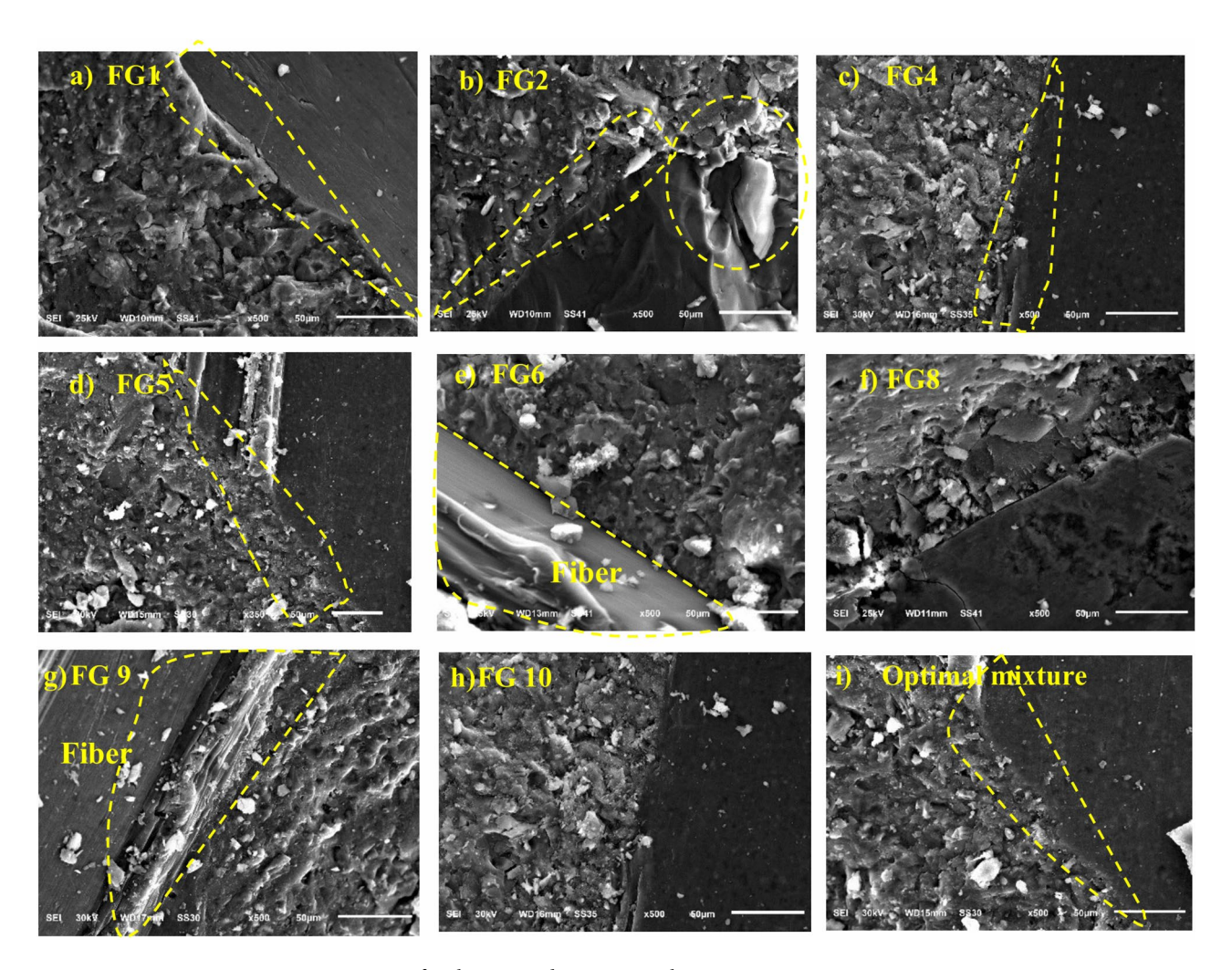


Fig. 17. SEM image of ambient cured HSGC samples.

contrast, FG6 (Fig. 17e) displays a less homogeneous microstructure and demonstrates a weaker bond between the geopolymer matrix and pumice particle compared to other mixtures, which adversely affects its mechanical properties. This weaker bond is attributed to the surface nature of the pumice particle (Fig. 1), which aligns with the findings of Karaaslan et al.<sup>25</sup> regarding the impact of pumice powder on the microstructure of GPC. The reduction in strength and the uncompacted microstructure of HSGC incorporating high contents of VPP can be attributed to increased porosity, which disrupts its homogeneity and connectivity and consequently leads to diminished structural integrity.

### Resistance to elevated temperature exposure Residual strength

Figure 18 presents the residual CSs of the optimized mixture (Table 8) and high strength (FG5), and low strength (FG6) samples after exposure to temperatures ranging from 200 to 800 °C. It shows that all mixtures experienced a strength gain after being exposed to 200 °C, with residual strengths varying between 107 and 116%. This increase in strength is likely due to additional reactions among the binder particles at this temperature. Abdellatief et al. 48 observed a similar phenomenon with GPC, which gained strength after exposure to 200 °C due to further geopolymerization. Similarly, Khan et al. 49 noted a slight increase in strength of alkali-activated concrete at 200 °C compared to their initial strength. Figure 18 also indicates that the residual CS trends of HSGC containing VPP after exposure to 200 °C and 400 °C were similar to those observed for mixtures cured at 60°C. However, HSGC with high volume of VPP demonstrated lower residual CS than the other samples when exposed to 600 °C and 800 °C. For example, after exposure to 800 °C, the residual CS for FG6 were 23.25%, while the optmized sample and FG5 had a residual strength of 27.38% and 29.28%, respectively. This increase in the residual strength of the FG5 sample was due to the BF inhibiting high-temperature cracking and limiting damage to the samples. These results are consistent with findings reported Guler et al. 50 and Ziada et al. 45.

Microstructural analysis at elevated temperature

The SEM images ( $100 \mu m$  and  $10 \mu m$ ) of the optimized mixture, FG5, and FG6 samples after exposure to  $800 \, ^{\circ}$ C are presented in Fig. 19 to assess the effects of VPP and BF under high-temperature conditions. The

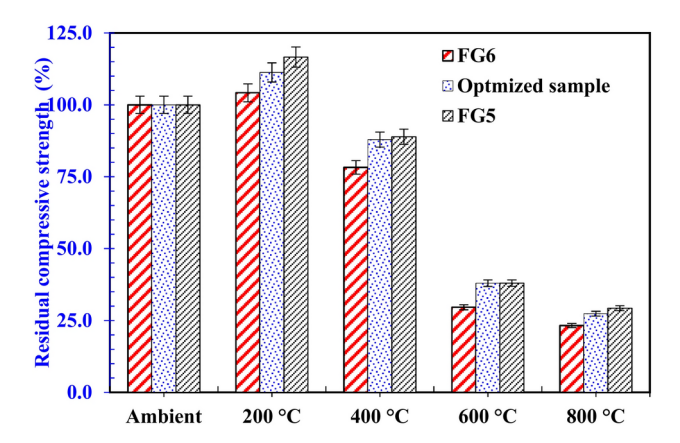


Fig. 18. Residual CSs of HSGC samples after elevated temperature exposure.

analysis revealed that at 800 °C, especially in sample FG6, the gel structures showed significant cracks and voids (Fig. 19a). Albidah et al.<sup>51</sup> attributed the strength loss in GPCs exposed to elevated temperatures to the formation of porous, sponge-like structures, while Topal et al.<sup>52</sup> observed intensified microstructural deterioration after 800 °C, linking it to corresponding reductions in strength. The microstructural analysis indicated that the number of voids and cracks increased, with micro-cracks becoming larger and more extensive at 800 °C. This damage compromised the microstructural integrity of the HSGC samples, resulting in a less stable appearance. In contrast, the FG5 sample exhibited fewer micro- and macro-cracks compared to FG6, as shown in Fig. 19c. This improvement is attributed to the BF fibers' capability to effectively control the rapid progression of cracks through their bridging effect, owing to their high tensile strength and elastic modulus, which enhance their adhesion to the matrix. Furthermore, the hybrid use of VPP and BA fibers was found to be more effective in reducing micro and macro cracks within the microstructures of HSGC compared to the FG6 sample (Fig. 19b). Finally, Fig. 19 demonstrates significant damage to the interfacial transition zone (ITZ) of the FG6 sample after exposure to 800 °C, likely due to the high volume of VPP, which creates pores in the ITZ and weakens the bond between the fibers and the geopolymer matrix. In contrast, Fig. 19b and c demonstrate that the optimized sample with optimal VPP content and high BF percentage in the FG5 samples forms a stronger connection with the geopolymer matrix at the ITZ after 800 °C exposure. Notably, the microstructure of FG5 is more homogeneous and less porous compared to the other mixtures.

#### **TG-DTG** analysis

The thermal stability of the samples was analyzed through TGA, emphasizing weight loss percentage as a function of temperature. The findings, illustrated in Fig. 20, include both TGA and DTG data for all samples. For the FG6 sample (Fig. 20a), a significant weight loss occurred from room temperature to 150 °C, primarily due to the evaporation of physically adsorbed water. The TGA curve for FG6 is notably steeper in this range, as indicated by the DTG graph, where FG6's peak appears at a lower temperature compared to the other mixtures. This behavior can be attributed to FG6's high porosity, stemming from its high content of VPP, which diminishes its capacity to retain water<sup>48</sup>. In contrast, the FG5 sample demonstrated the highest thermal stability among the geopolymer samples. The peak of the optimized mixture (Fig. 20b) shifted slightly to a higher temperature, likely due to the effective filling of voids by optimal VPP content, resulting in a denser geopolymer. Additionally, the pozzolanic characteristics of pumice particles and the optimal blend of BF likely contributed to a more stable structure at elevated temperatures. As interstitial water—potentially linked to sodium cations—started to decompose and physical free water had evaporated, the weight loss rate for all samples began to slow between 150 and 300 °C. The gradual mass loss observed between 300 and 600 °C is linked to the de-hydroxylation of chemically bound silicon-hydroxyl groups, forming Si-O-Si bridges with the release of water (2Si-OH→Si-O-Si+H<sub>2</sub>O↑)<sup>48,52</sup>. From 600 to 700 °C, weight loss was minimal, attributed to the combustion of remnants from GGBS and VPP. At 800 °C, total weight losses for the FG6 (Fig. 20a), optimized mixture (Fig. 20b), and FG5 (Fig. 20c) samples ranged from 7.0% to 8.16%. Specifically, FG6 retained less than 91.84% of its weight under elevated temperatures, while the optimized mixture and FG5 retained around 93.0%. This suggests that the optimized mixture exhibited a hydration level comparable to that of FG5 at elevated temperatures, thereby demonstrating superior thermal stability compared to the FG6 sample.

### **Conclusions**

- 1. The addition of BF significantly enhances compressive, flexural, and splitting strengths. Specifically, increasing BF content from 0.75 to 1.5% results in notable strength improvements, with CS increasing by up to 14.51% at 28 days and flexural and splitting strengths improving by up to 13.17% and 14.46%, respectively. Additionally, incorporating VPP generally reduces compressive strength, particularly at higher concentrations, with a notable reduction of 23% at 40% VPP after 7 days.
- 2. Evaporation drives excess alkali solutions to the surface, where they react with atmospheric CO<sub>2</sub> to form carbonates. This indicates that, despite the consumption of alkali during geopolymerization, a significant re-

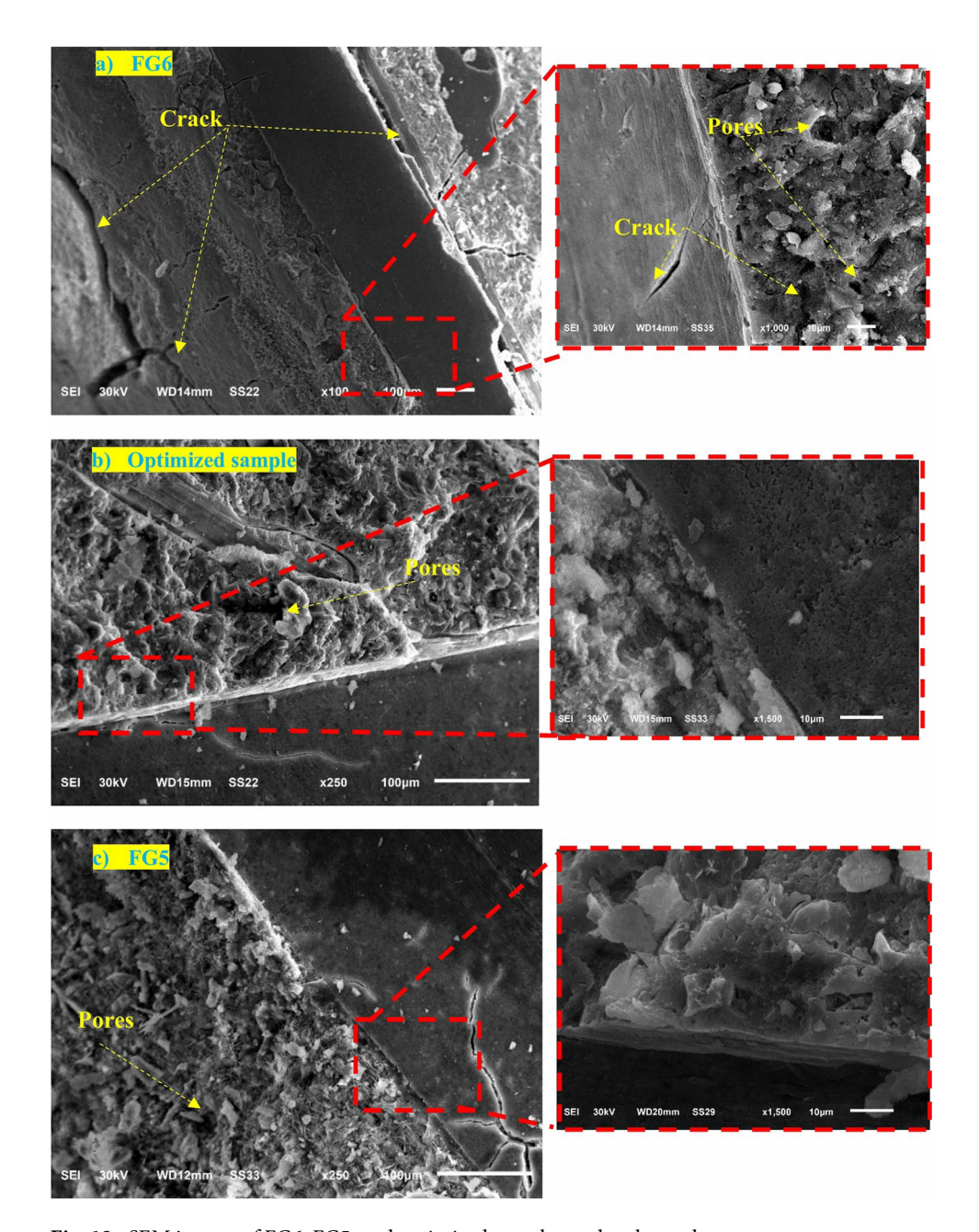
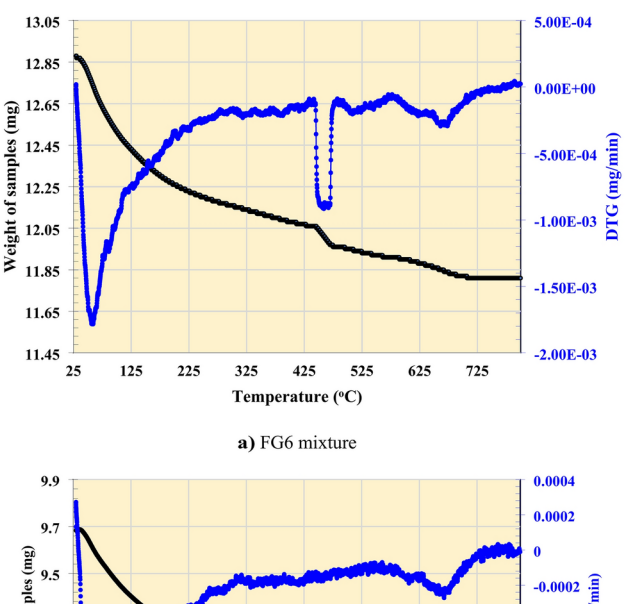
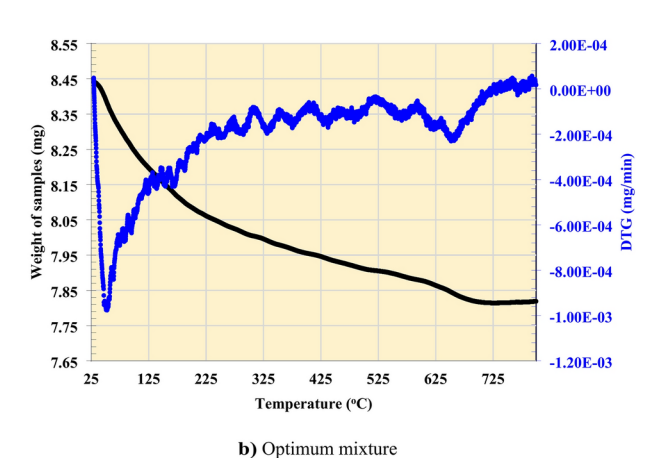


Fig. 19. SEM images of FG6, FG5, and optimized samples under elevated temperatures.

sidual amount remains, posing a risk for efflorescence. The composition of the geopolymer mix is significant; particularly, varying levels of VPP negatively influence efflorescence dynamics, with increased VPP content associated with a greater formation of white crystals on the surface.

- 3. The optimal mixture (17.79% VPP and 0.69% BF) and FG5 mixture exhibited superior residual strength after exposure to elevated temperatures, particularly at 800 °C. Additionally, this mixture achieved a slump of 107 mm, a dry density of 2012 kg/m $^3$ , a compressive strength of 59.25 MPa, a flexural strength of 8.64 MPa, and a splitting tensile strength of 7.51 MPa.
- 4. SEM and thermal analyses of the optimal mixture reveal a dense and homogeneous microstructure with enhanced gel formation and stability at high temperatures. These findings align with improved mechanical performance, validating the effectiveness of the optimized mix design. These points collectively indicate the importance of careful optimization of BF and VPP content to enhance the performance of HSGC, while balancing strengths and addressing potential issues like efflorescence and elevated temperature resistance.
- 5. This study shows that BF significantly increases thermal resistance in HSGC because FG5 retains the highest residual CS (29.28%) at 800 °C. The bridging effect of BF effectively inhibits fracture propagation and preserves microstructural integrity, whereas excessive VPP results in increased porosity and weaker ITZ, which exacerbate strength deterioration.





9.3 -0 0006 9.1 -0.0008 8.9 -0.001 -0.0012 125 425 525 625 725 25 225 325 Temperature (°C) c) FG5 mixture

Fig. 20. TGA/DTG results of the HSGC.

6. The improved geopolymer mixture showed superior thermal stability, retaining about 93.0% of its weight at 800 °C, comparable to FG5, while FG6 only retained 91.84%. The optimal VPP content is in charge of this enhanced stability by effectively reducing porosity and improving the geopolymer matrix's resistance to thermal degradation, highlighting the critical role that material composition plays in high-temperature performance.

#### Data availability

The datasets used and/or analysed during the current study available from the corresponding author on reasonable request.

Received: 21 October 2024; Accepted: 14 April 2025

Published online: 27 April 2025

#### References

- 1. Adamu, M., Alanazi, H., Ibrahim, Y. E. & Abdellatief, M. Mechanical, microstructural characteristics and sustainability analysis of concrete incorporating date palm ash and eggshell powder as ternary blends cementitious materials. *Constr. Build. Mater.* 411, 134753. https://doi.org/10.1016/J.CONBUILDMAT.2023.134753 (2024).
- Shekhawat, P., Sharma, G. & Singh, R. M. Microstructural and morphological development of eggshell powder and flyash-based geopolymers. Constr. Build. Mater. 260, 119886. https://doi.org/10.1016/J.CONBUILDMAT.2020.119886 (2020).
- Xiao, R. et al. Strength, microstructure, efflorescence behavior and environmental impacts of waste glass geopolymers cured at ambient temperature. J. Clean Prod. 252, 119610. https://doi.org/10.1016/J.JCLEPRO.2019.119610 (2020).
- Guan, X. et al. Ultra-high early strength fly ash-based geopolymer paste cured by microwave radiation. Dev. Built Environ. 14, 100139. https://doi.org/10.1016/J.DIBE.2023.100139 (2023).
- Abdellatief, M. et al. Physico-mechanical, thermal insulation properties, and microstructure of geopolymer foam concrete containing sawdust ash and egg shell. J. Build. Eng. 90, 109374. https://doi.org/10.1016/J.JOBE.2024.109374 (2024).
- Jaya, N. A., Yun-Ming, L., Cheng-Yong, H., Abdullah, M. M. A. B. & Hussin, K. Correlation between pore structure, compressive strength and thermal conductivity of porous metakaolin geopolymer. *Constr. Build. Mater.* 247, 118641. https://doi.org/10.1016/J. CONBUILDMAT.2020.118641 (2020).
- 7. Cai, R., Wu, T., Fu, C. & Ye, H. Thermal degradation of potassium-activated ternary slag-fly ash-silica fume binders. Constr. Build. Mater. 320, 126304. https://doi.org/10.1016/J.CONBUILDMAT.2021.126304 (2022).
- Ranjbar, N. & Zhang, M. Fiber-reinforced geopolymer composites: A review. Cem. Concr. Compos. 107, 103498. https://doi.org/1 0.1016/J.CEMCONCOMP.2019.103498 (2020).
- Ozcelikci, E., Ozdogru, E., Tugluca, M. S., Ilcan, H. & Sahmaran, M. Comprehensive investigation of performance of construction and demolition waste based wood fiber reinforced geopolymer composites. *J. Build. Eng.* 84, 108682. https://doi.org/10.1016/J.JO BE.2024.108682 (2024).

- Khouchani, O., Harmal, A., El-Korchi, T., Tao, M. & Walker, H. W. Effect of cellulose nanocrystals on performance of PVA fiber-reinforced geopolymer composites: Reaction kinetics, bending behavior, and toughening mechanisms. Constr. Build. Mater. 435, 136727. https://doi.org/10.1016/J.CONBUILDMAT.2024.136727 (2024).
- 11. Islam, A. et al. Influence of steel fibers on the mechanical properties and impact resistance of lightweight geopolymer concrete. Constr. Build Mater. 152, 964–977. https://doi.org/10.1016/J.CONBUILDMAT.2017.06.092 (2017).
- Behera, P., Baheti, V., Militky, J. & Naeem, S. Microstructure and mechanical properties of carbon microfiber reinforced geopolymers at elevated temperatures. Constr. Build. Mater. 160, 733–743. https://doi.org/10.1016/J.CONBUILDMAT.2017.11.109 (2018).
- 13. Wang, Y., Hu, S. & Sun, X. Experimental investigation on the elastic modulus and fracture properties of basalt fiber-reinforced fly ash geopolymer concrete. *Constr. Build. Mater.* 338, 127570. https://doi.org/10.1016/J.CONBUILDMAT.2022.127570 (2022).
- 14. Asil, M. B. & Ranjbar, M. M. Hybrid effect of carbon nanotubes and basalt fibers on mechanical, durability, and microstructure properties of lightweight geopolymer concretes. *Constr. Build. Mater.* 357, 129352. https://doi.org/10.1016/J.CONBUILDMAT.20 22.129352 (2022).
- 15. Yang, W. et al. A review of the mechanical properties and durability of basalt fiber recycled concrete. *Constr. Build. Mater.* **412**, 134882. https://doi.org/10.1016/J.CONBUILDMAT.2024.134882 (2024).
- Branston, J., Das, S., Kenno, S. Y. & Taylor, C. Mechanical behaviour of basalt fibre reinforced concrete. Constr. Build. Mater. 124, 878–886. https://doi.org/10.1016/J.CONBUILDMAT.2016.08.009 (2016).
- 17. Zhang, T., Wang, K., Lin, B. & Yao, Y. The enhancement mechanism of modified basalt fiber on the performance of geopolymer concrete. Constr. Build. Mater. 417, 135123. https://doi.org/10.1016/J.CONBUILDMAT.2024.135123 (2024).
- Sohail, M. G., Alnahhal, W., Taha, A. & Abdelaal, K. Sustainable alternative aggregates: Characterization and influence on mechanical behavior of basalt fiber reinforced concrete. Constr. Build. Mater. 255, 119365. https://doi.org/10.1016/J.CONBUILD MAT.2020.119365 (2020).
- Alnahhal, W., Taha, R., Alnuaimi, N. & Al-Hamrani, A. Properties of fibre-reinforced concrete made with discarded materials. Mag. Concr. Res. 71, 152–162. https://doi.org/10.1680/jmacr.17.00293 (2019).
- Zhang, C., Hao, H. & Hao, Y. Experimental study of mechanical properties of double-helix BFRP fiber reinforced concrete at high strain rates. Cem. Concr. Compos. 132, 104633. https://doi.org/10.1016/J.CEMCONCOMP.2022.104633 (2022).
- Li, N. et al. A mixture proportioning method for the development of performance-based alkali-activated slag-based concrete. Cem. Concr. Compos. 93, 163–174. https://doi.org/10.1016/J.CEMCONCOMP.2018.07.009 (2018).
- Saif, M. S., El-Hariri, M. O. R., Sarie-Eldin, A. I., Tayeh, B. A. & Farag, M. F. Impact of Ca+ content and curing condition on durability performance of metakaolin-based geopolymer mortars. Case Stud. Constr. Mater. 16, e00922. https://doi.org/10.1016/J. CSCM.2022.E00922 (2022).
- Redden, R. & Neithalath, N. Microstructure, strength, and moisture stability of alkali activated glass powder-based binders. Cem. Concr. Compos. 45, 46–56. https://doi.org/10.1016/J.CEMCONCOMP.2013.09.011 (2014).
- Nasaeng, P., Wongsa, A., Cheerarot, R., Sata, V. & Chindaprasirt, P. Strength enhancement of pumice-based geopolymer paste by incorporating recycled concrete and calcined oyster shell powders. Case Stud. Constr. Mater. 17, e01307. https://doi.org/10.1016/J .CSCM.2022.F01307 (2022).
- 25. Karaaslan, C., Yener, E., Bağatur, T. & Polat, R. Improving the durability of pumice-fly ash based geopolymer concrete with calcium aluminate cement. *J. Build. Eng.* **59**, 105110. https://doi.org/10.1016/J.JOBE.2022.105110 (2022).
- Zeyad, A. M. et al. Production of geopolymer concrete by utilizing volcanic pumice dust. Case Stud. Constr. Mater. 16, e00802. https://doi.org/10.1016/J.CSCM.2021.E00802 (2022).
- Safari, Z., Kurda, R., Al-Hadad, B., Mahmood, F. & Tapan, M. Mechanical characteristics of pumice-based geopolymer paste. Resour. Conserv. Recycl. 162, 105055. https://doi.org/10.1016/J.RESCONREC.2020.105055 (2020).
- Tahwia, A. M., Aldulaimi, D. S., Abdellatief, M. & Youssf, O. Physical, mechanical and durability properties of eco-friendly engineered geopolymer composites. *Infrastructures* https://doi.org/10.3390/infrastructures9110191 (2024).
- 29. Safari, Z., Younis, K. H. & Kamal, I. Sustainable utilization of waste pumice powder in slag-based geopolymer concretes: fresh and mechanical properties. Sustainability https://doi.org/10.3390/su16219296 (2024).
- 30. Srinivasamurthy, L. et al. Mechanical property and microstructure development in alkali activated fly ash slag blends due to efflorescence. Constr. Build. Mater. 332, 127273. https://doi.org/10.1016/J.CONBUILDMAT.2022.127273 (2022).
- 31. Longhi, M. A. et al. New selective dissolution process to quantify reaction extent and product stability in metakaolin-based geopolymers. *Compos. B. Eng.* 176, 107172. https://doi.org/10.1016/J.COMPOSITESB.2019.107172 (2019).
- 32. Elfadaly, E., Othman, A. M., Aly, M. H., Elgarhy, W. A. & Abdellatief, M. Assessing performance and environmental benefits of high-performance geopolymer mortar incorporating pumice and rice straw ash. *Sustain. Chem. Pharm.* 44, 101918. https://doi.org/10.1016/J.SCP.2025.101918 (2025).
- 33. Abdellatief, M., Elrahman, M. A., Abadel, A. A., Wasim, M. & Tahwia, A. Ultra-high performance concrete versus ultra-high performance geopolymer concrete: Mechanical performance, microstructure, and ecological assessment. *J. Build. Eng.* **79**, 107835. https://doi.org/10.1016/J.JOBE.2023.107835 (2023).
- 34. Abdellatief, M., Elrahman, M. A., Elgendy, G., Bassioni, G. & Tahwia, A. M. Response surface methodology-based modelling and optimization of sustainable UHPC containing ultrafine fly ash and metakaolin. *Constr. Build. Mater.* 388, 131696. https://doi.org/10.1016/J.CONBUILDMAT.2023.131696 (2023).
- Ghelich, R., Jahannama, M. R., Abdizadeh, H., Torknik, F. S. & Vaezi, M. R. Central composite design (CCD)-Response surface methodology (RSM) of effective electrospinning parameters on PVP-B-Hf hybrid nanofibrous composites for synthesis of HfB2based composite nanofibers. *Compos. B. Eng.* 166, 527–541. https://doi.org/10.1016/J.COMPOSITESB.2019.01.094 (2019).
- 36. Almohammed, F., Thakur, M. S., Lee, D., Kumar, R. & Singh, T. Flexural and split tensile strength of concrete with basalt fiber: An experimental and computational analysis. *Constr. Build. Mater.* 414, 134936. https://doi.org/10.1016/J.CONBUILDMAT.2024.134 936 (2024).
- 37. Zhang, C., Wang, Y., Zhang, X., Ding, Y. & Xu, P. Mechanical properties and microstructure of basalt fiber-reinforced recycled concrete. *J. Clean. Prod.* 278, 123252. https://doi.org/10.1016/J.JCLEPRO.2020.123252 (2021).
- 38. Huang, M., Zhao, Y., Wang, H. & Lin, S. Mechanical properties test and strength prediction on basalt fiber reinforced recycled concrete. Adv. Civ. Eng. 2021, 6673416. https://doi.org/10.1155/2021/6673416 (2021).
- Katkhuda, H. & Shatarat, N. Improving the mechanical properties of recycled concrete aggregate using chopped basalt fibers and acid treatment. Constr. Build. Mater. 140, 328–335. https://doi.org/10.1016/J.CONBUILDMAT.2017.02.128 (2017).
- Alnahhal, W. & Aljidda, O. Flexural behavior of basalt fiber reinforced concrete beams with recycled concrete coarse aggregates. Constr. Build. Mater. 169, 165–178. https://doi.org/10.1016/J.CONBUILDMAT.2018.02.135 (2018).
- 41. Ismail, I. et al. Modification of phase evolution in alkali-activated blast furnace slag by the incorporation of fly ash. *Cem. Concr. Compos.* 45, 125–135. https://doi.org/10.1016/J.CEMCONCOMP.2013.09.006 (2014).
- 42. Karaaslan, C. et al. Synergic effect of fly ash and calcium aluminate cement on the properties of pumice-based geopolymer mortar. Constr. Build. Mater. 345, 128397. https://doi.org/10.1016/J.CONBUILDMAT.2022.128397 (2022).
- 43. Zhao, Q. et al. Effect of silica fume on the efflorescence, strength, and micro-properties of one-part geopolymer incorporating sewage sludge ash. Constr. Build. Mater. 436, 136840. https://doi.org/10.1016/J.CONBUILDMAT.2024.136840 (2024).
- Smarzewski, P. Influence of basalt-polypropylene fibres on fracture properties of high performance concrete. Compos. Struct. 209, 23–33. https://doi.org/10.1016/J.COMPSTRUCT.2018.10.070 (2019).

- 45. Ziada, M., Erdem, S., Tammam, Y., Kara, S. & Lezcano, R. A. G. The effect of basalt fiber on mechanical, microstructural, and hightemperature properties of fly ash-based and basalt powder waste-filled sustainable geopolymer mortar. Sustainability https://doi.o rg/10.3390/su132212610 (2021).
- 46. Walkley, B. et al. Phase evolution of C-(N)-A-S-H/N-A-S-H gel blends investigated via alkali-activation of synthetic calcium aluminosilicate precursors. Cem. Concr. Res. 89, 120-135. https://doi.org/10.1016/J.CEMCONRES.2016.08.010 (2016).
- 47. Xu, J., Kang, A., Wu, Z., Xiao, P. & Gong, Y. Effect of high-calcium basalt fiber on the workability, mechanical properties and microstructure of slag-fly ash geopolymer grouting material. Constr. Build. Mater. 302, 124089. https://doi.org/10.1016/j.conbuild mat.2021.124089 (2021).
- 48. Tahwia, A. M., Ellatief, M. A., Bassioni, G., Heniegal, A. M. & Elrahman, M. A. Influence of high temperature exposure on compressive strength and microstructure of ultra-high performance geopolymer concrete with waste glass and ceramic. J. Market. Res. 23, 5681-5697. https://doi.org/10.1016/J.JMRT.2023.02.177 (2023).
- 49. Khan, M. N. N. & Sarker, P. K. Effect of waste glass fine aggregate on the strength, durability and high temperature resistance of alkali-activated fly ash and GGBFS blended mortar. Constr. Build. Mater. 263, 120177. https://doi.org/10.1016/J.CONBUILDMAT 2020 120177 (2020)
- 50. Guler, S. & Akbulut, Z. F. Effect of high-temperature on the behavior of single and hybrid glass and basalt fiber added geopolymer cement mortars. J. Build. Eng. 57, 104809. https://doi.org/10.1016/j.jobe.2022.104809 (2022).
- 51. Albidah, A., Algarni, A. S., Abbas, H., Almusallam, T. & Al-Salloum, Y. Behavior of metakaolin-based geopolymer concrete at ambient and elevated temperatures. Constr. Build. Mater. 317, 125910. https://doi.org/10.1016/j.conbuildmat.2021.125910 (2022).
- 52. Topal, Ö., Karakoç, M. B. & Özcan, A. Effects of elevated temperatures on the properties of ground granulated blast furnace slag (GGBFS) based geopolymer concretes containing recycled concrete aggregate. Eur. J. Environ. Civ. Eng. 26, 4847–4862. https://do i.org/10.1080/19648189.2021.1871658 (2022).

#### Acknowledgements

The authors acknowledge the European project 5RP: RFCS-01-2022-RPJ; RFCS-PJG, "New technology for hydrogen and geopolymer composites production from post-mining waste" - H2GEO No 101112386.

#### **Author contributions**

Mohamed Abdellatief and Taher A. Tawfik: Conceptualization, analysis of data, writing-reviewing and editing. Hassan Hamouda and Martin T. Palou: Methodology, experimental part, writing- original draft preparation. Mohamed Abdellatief and Martin T. Palou: Visualization, writing- reviewing and editing, Taher A. Tawfik and Mohamed Abdellatief: rewriting- reviewing and editing.

#### **Declarations**

#### Competing interests

The authors declare no competing interests.

#### Additional information

Correspondence and requests for materials should be addressed to T.A.T.

Reprints and permissions information is available at www.nature.com/reprints.

Publisher's note Springer Nature remains neutral with regard to jurisdictional claims in published maps and institutional affiliations.

Open Access This article is licensed under a Creative Commons Attribution-NonCommercial-NoDerivatives 4.0 International License, which permits any non-commercial use, sharing, distribution and reproduction in any medium or format, as long as you give appropriate credit to the original author(s) and the source, provide a link to the Creative Commons licence, and indicate if you modified the licensed material. You do not have permission under this licence to share adapted material derived from this article or parts of it. The images or other third party material in this article are included in the article's Creative Commons licence, unless indicated otherwise in a credit line to the material. If material is not included in the article's Creative Commons licence and your intended use is not permitted by statutory regulation or exceeds the permitted use, you will need to obtain permission directly from the copyright holder. To view a copy of this licence, visit http://creativecommo ns.org/licenses/by-nc-nd/4.0/.

© The Author(s) 2025